

JGR Space Physics

RESEARCH ARTICLE

10.1029/2020JA029081

Special Section:

Geospace multi-point observations in Van Allen Probes and Arase era

Key Points:

- Heat fluxes estimated from Radiation Belt Storm Probes (RBSP) reached the order of 10^9 eV/cm²/s, indicating that Coulomb collisions could be the cause of stable auroral red (SAR) arcs
- The RBSP-A satellite observed local enhancements of 7–20-mHz electromagnetic wave power above a SAR arc
- Arase observed increases of electron fluxes (<200 eV) and various electromagnetic waves above a freshly detached SAR arc

Supporting Information:

Supporting Information may be found in the online version of this article.

Correspondence to:

Y. Inaba,
inaba.yudai@isee.nagoya-u.ac.jp












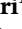


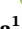






Citation:

Inaba, Y., Shiokawa, K., Oyama, S., Otsuka, Y., Connors, M., Schofield, I., et al. (2021). Multi-event analysis of plasma and field variations in source of stable auroral red (SAR) arcs in inner magnetosphere during non-storm-time substorms. *Journal of Geophysical Research: Space Physics*, 126, e2020JA029081. <https://doi.org/10.1029/2020JA029081>

Received 5 JAN 2021

Accepted 4 MAR 2021

Multi-Event Analysis of Plasma and Field Variations in Source of Stable Auroral Red (SAR) Arcs in Inner Magnetosphere During Non-Storm-Time Substorms

Yudai Inaba¹ , Kazuo Shiokawa¹ , Shin-ichiro Oyama^{1,2,3} , Yuichi Otsuka¹ , Martin Connors⁴ , Ian Schofield⁴ , Yoshizumi Miyoshi¹ , Shun Imajo¹ , Atsuki Shinbori¹ , Artem Yu Gololobov⁵ , Yoichi Kazama⁶ , Shiang-Yu Wang⁶ , Sunny W. Y. Tam⁷ , Tzu-Fang Chang⁷ , Bo-Jhou Wang⁶ , Kazushi Asamura⁸ , Shoichiro Yokota⁹ , Satoshi Kasahara¹⁰ , Kunihiro Keika¹⁰ , Tomoaki Hori¹ , Ayako Matsuoka¹¹ , Yoshiya Kasahara¹² , Atsushi Kumamoto¹³ , Shoya Matsuda⁸ , Yasumasa Kasaba¹³ , Fuminori Tsuchiya¹³ , Masafumi Shoji¹ , Masahiro Kitahara¹ , Satoko Nakamura¹ , Iku Shinohara⁸ , Harlan E. Spence¹⁴ , Geoff D. Reeves¹⁵ , Robert J. Macdowall¹⁶ , Charles W. Smith¹⁴ , John R. Wygant¹⁷ , and John W. Bonnell¹⁸ 

¹Institute for Space-Earth Environmental Research, Nagoya University, Nagoya, Japan, ²Space Physics and Astronomy Research Unit, University of Oulu, Oulu, Finland, ³National Institute of Polar Research, Tokyo, Japan, ⁴Athabasca University Observatories, Athabasca University, Athabasca, AB, Canada, ⁵Laboratory of Magnetospheric and Ionospheric research, Yu.G. Shafer Institute of Cosmophysical Research and Aeronomy of Siberian Branch of the Russian Academy of Sciences, Yakut Scientific Centre of Siberian Branch of the Russian Academy of Sciences, Yakutsk, Russia, ⁶Academia Sinica Institute of Astronomy and Astrophysics, Taipei, Taiwan, ⁷Institute of Space and Plasma Sciences, National Cheng Kung University, Tainan, Taiwan, ⁸Institute of Space and Astronautical Science, Kanagawa, Japan, ⁹Department of Earth and Space Science, Graduate School of Science, Osaka University, Toyonaka, Japan, ¹⁰Department of Earth and Planetary Science, School of Science, The University of Tokyo, Tokyo, Japan, ¹¹Graduate School of Science, Data Analysis Center for Geomagnetism and Space Magnetism, Kyoto University, Kyoto, Japan, ¹²Graduate School of Natural Science and Technology, Kanazawa University, Kanazawa, Japan, ¹³Graduate School of Science, Tohoku University, Sendai, Japan, ¹⁴Institute for the Study of Earth, Oceans, and Space, University of New Hampshire, Durham, NH, USA, ¹⁵Space and Atmospheric Sciences, Los Alamos National Laboratory, Los Alamos, NM, USA, ¹⁶NASA Goddard Space Flight Center, Greenbelt, MD, USA, ¹⁷Physics and Astronomy, University of Minnesota, Minneapolis, MN, USA, ¹⁸Space Sciences Laboratory, University of California, Berkeley, CA, USA

Abstract Stable auroral red (SAR) arcs are optical events with dominant 630.0-nm emission caused by low-energy electron heat flux into the topside ionosphere from the inner magnetosphere. SAR arcs are observed at subauroral latitudes and often occur during the recovery phase of magnetic storms and substorms. Past studies concluded that these low-energy electrons were generated in the spatial overlap region between the outer plasmasphere and ring-current ions and suggested that Coulomb collisions between plasmaspheric electrons and ring-current ions are more feasible for the SAR-arc generation mechanism rather than Landau damping by electromagnetic ion cyclotron waves or kinetic Alfvén waves. This work studies three separate SAR-arc events with conjunctions, using all-sky imagers and inner magnetospheric satellites (Arase and Radiation Belt Storm Probes [RBSP]) during non-storm-time substorms on December 19, 2012 (event 1), January 17, 2015 (event 2), and November 4, 2019 (event 3). We evaluated for the first time the heat flux via Coulomb collision using full-energy-range ion data obtained by the satellites. The electron heat fluxes due to Coulomb collisions reached $\sim 10^9$ eV/cm²/s for events 1 and 2, indicating that Coulomb collisions could have caused the SAR arcs. RBSP-A also observed local enhancements of 7–20-mHz electromagnetic wave power above the SAR arc in event 2. The heat flux for the freshly detached SAR arc in event 3 reached $\sim 10^8$ eV/cm²/s, which is insufficient to have caused the SAR arc. In event 3, local flux enhancement of electrons (<200 eV) and various electromagnetic waves were observed, these are likely to have caused the freshly detached SAR arc.

Plain Language Summary Stable auroral red (SAR) arcs are aurora with an optical red emission from oxygen atoms at latitudes slightly lower than the auroral oval and often occur during storm-time substorms. The oxygen excitation is caused by low-energy electrons transferred from the inner magnetosphere to the ionosphere. Past studies concluded that these low-energy electrons were generated

in the spatial overlap region between the plasmaspheric cold electrons and high-energy ring-current ions and suggested that Coulomb collisions are more plausible as the generation mechanism of SAR arcs than are electromagnetic waves. In this study, we report three SAR-arc events observed by all-sky imagers and inner magnetospheric satellites (Arase and Radiation Belt Storm Probes). We evaluated for the first time the three possible activation mechanisms using the data for full-energy-range plasma and electromagnetic wave data obtained by the satellites. As predicted previously, the calculated heat flux could have caused the SAR arcs in two of the events, but there were mixed cases in which electromagnetic waves were observed. When Arase flew above a freshly generated SAR arc, the flux of low-energy electrons (<200 eV) was enhanced and various electromagnetic waves were observed, which may be responsible for its generation.

1. Introduction

Stable auroral red (SAR) arcs with 630.0-nm emission are caused by low-energy electron heat flux or precipitation from the inner magnetosphere into the topside ionosphere. SAR arcs are observed at subauroral latitudes equatorward of the auroral oval and often occur during the recovery phase of magnetic storms and substorms (e.g., Rees & Roble, 1975; Takagi et al., 2018). SAR arcs have long been investigated since their discovery in the 1950s (Barbier, 1958). Roach and Roach (1963) reported that the average altitude of the peak intensity of the 630.0-nm emission was 400 km. Foster et al. (1994) found that the ionospheric trough and the subauroral ion drift occurred simultaneously in the SAR-arc region. Shiokawa et al. (2013) showed a SAR-arc event during the initial phase of a geomagnetic storm. They concluded that the SAR arc was caused by the inward movement of the ring current induced by storm-time substorms. Mendillo et al. (2016) showed that a SAR arc developed zonally from east to west, and the arc was accompanied by a weak 557.7-nm patchy emission. Shiokawa et al. (2009, 2017) and Takagi et al. (2018) reported the detachment of SAR arcs from the auroral oval toward lower latitudes associated with substorm recovery. Takagi et al. (2018) showed statistically that the arc detachment occurs mainly in the pre-midnight sector. In recent years, it has also been suggested that SAR arcs are associated with strong thermal emission velocity enhancement (STEVE), which is also an emission structure at subauroral latitudes (e.g., MacDonald et al., 2018; Mendillo et al., 2019). Oyama et al. (2020) showed “ephemeral red arc” phenomena observed during a geomagnetically quiet period ($K_p = 0+$) and suggested that such arcs may represent the birth of SAR arcs related to the substorm particle injection.

There are three possible mechanisms in the magnetosphere that could generate low-energy electrons to cause SAR arcs. The first is Coulomb collisions between plasmaspheric cold electrons/ions and ring-current hot ions (e.g., Cole, 1965; Ievenko, 2020; Kozyra et al., 1987). The energy is transferred to the upper atmosphere via heat conduction or as a low-energy electron flux (e.g., Prölss, 2006). The second is the Landau damping of electromagnetic ion cyclotron (EMIC) waves to cause heated electrons to precipitate into the ionosphere (e.g., Cornwall et al., 1971; B. Wang et al., 2019; Zhou et al., 2013). Although it was not a simultaneous observation with a SAR arc, Yuan et al. (2014) used Cluster satellite data to show that the electrons of a plasma plume were heated by the Landau damping of EMIC waves. The third is kinetic Alfvén waves (KAWs) with the electric field parallel to the magnetic field to accelerate plasmaspheric cold electrons to the upper atmosphere (Hasegawa & Mima, 1978). Lanzerotti et al. (1978) reported a SAR arc that occurred simultaneously with hydromagnetic waves at a frequency of ~ 10 mHz measured by ground-based measurements; they suggested that sufficient wave energy was available for electron heating in their SAR-arc event.

It has been reported observationally that SAR arcs are geomagnetically conjugate between the Northern and Southern Hemispheres (Martinis et al., 2019). Mendillo et al. (2019) showed that the emission intensities of SAR arcs observed at magnetically conjugate points differed between the hemispheres, and they explained the difference as being due to the seasonal variation of ambient electron density. The magnetic conjugacy of SAR arcs implies a physical process in the magnetosphere causing the arcs. It is thus essential to observe a conjugate site of the magnetosphere in order to identify what process is responsible for the SAR-arc generation. However, to date there have been only a few observations of the magnetospheric source region of SAR arcs (e.g., Chu et al., 2019; Ievenko, 2020; Inaba et al., 2020).

Kozyra et al. (1987, 1993) evaluated the electron heat flux due to Coulomb collisions using ring-current ion data from the DE-1 satellite and ambient electron density data from an ionospheric model; they concluded that H^+ and O^+ of the ring current are dominant sources for plasmaspheric electron heating to cause SAR arcs during the early and late recovery phases of storms, respectively. Recently, two observations of the magnetospheric source region of SAR arcs have been reported. Chu et al. (2019) reported a conjunction event of a STEVE and a SAR arc with ground-based all-sky imagers (ASIs) and Radiation Belt Storm Probes (RBSP)-B. They showed that the SAR-arc location corresponded to the overlap region between the outer plasmasphere and the ring current in the magnetospheric source. Inaba et al. (2020) studied a conjunction event of a SAR arc using a ground-based ASI and the Arase satellite. They found no EMIC waves or KAWs in association with the SAR arc in the source region of the magnetosphere, and suggested that Coulomb collisions were the most plausible mechanism on the basis of the measured ion fluxes and ambient electron densities. However, at the time of the SAR arc crossing, the Arase satellite was located significantly away (-33° in magnetic latitude) from the magnetic equator, and hence, their study cannot exclude a possibility that the waves were dampened before reaching the satellite. In addition, because of the lack of low-energy ion data below 5 keV/q from this event, the evaluation of Coulomb collisions was carried out using only high-energy ions with more than 5 keV/q (where the “q” indicates the amount of charge).

In this study, we show three conjunction events of SAR arcs observed by ground-based ASIs and inner magnetospheric satellites, namely, Arase and RBSP, during non-storm-time substorms on December 19, 2012 (event 1), January 17, 2015 (event 2), and November 4, 2019 (event 3). In each event, the satellite observations were made near the magnetic equatorial plane, and we estimate heat fluxes including ion flux data at energies below 5 keV/q. Therefore, it is possible to account for low-energy ion processes and electromagnetic waves near the equatorial plane better than our previous study (Inaba et al., 2020). Additionally, the conjunction events in the present study provide a good opportunity to learn about plasma and field characteristics in the magnetospheric source region of SAR arcs.

2. Instruments

2.1. Optical Mesosphere Thermosphere Imagers

We used the cooled-CCD ASIs (imagers 7 and 19) that are parts of the Optical Mesosphere Thermosphere Imagers (Shiokawa et al., 1999, 2000) installed at Athabasca, Canada ($54.60^\circ N$, $246.36^\circ E$; magnetic latitude [MLAT]: $61.1^\circ N$) and Gakona, Alaska ($62.39^\circ N$, $214.78^\circ E$; MLAT: $63.6^\circ N$), respectively. The installation of these imagers were conducted by the PWING (Study of dynamical variation of particles and waves in the inner magnetosphere using ground-based network observations) project (Shiokawa et al., 2017). These observatories are located at subauroral latitudes. Imager 7 (Athabasca) has five optical filters for emissions at the wavelengths of 557.7 nm (oxygen atoms, exposure time 5 s), 630.0 nm (oxygen atoms, 30 s), 720–910 nm (OH-bands, 1 s), 486.1 nm (hydrogen atoms, 40 s), 572.5 nm (background continuous emission, 15 s), 844.6 nm (oxygen atoms, 25 s), and 589.3 nm (sodium atoms, 15 s). The cadence of imager 7 for the OH-band was 10 min, and for other filters are 2 min. Imager 19 (Gakona) has five optical filters for emissions at the wavelengths of 557.7 nm (exposure time 15 s), 630.0 nm (30 s), 720–1,000 nm (OH band, 1 s), 486.1 nm (30 s), and 572.5 nm (30 s). Its cadence of imager 19 for the OH-band was also 10 min, but for other filters 1.5 min. These filters transmit a narrow passband (transmission width: 1.5–2.0 nm) of specific lines of aurora and night airglow. The 557.7-nm and 630.0-nm images were used to analyze the aurora/airglow emissions. The imagers were calibrated to derive the absolute emission intensity using the optical facilities at the National Institute of Polar Research, Japan (Ogawa et al., 2020; Shiokawa et al., 2000). The weather conditions for events 1–3 were clear sky, cloudy followed by clear sky, and cloudy followed by clear sky with a few clouds, respectively.

2.2. Exploration of Energization and Radiation in Geospace

The Exploration of energization and Radiation in Geospace (ERG, also called Arase) satellite (Miyoshi, Shinohara, Takashima, et al., 2018) is in an elliptical earth orbit with an inclination of 31° at a distance of ~ 400 – $32,000$ km with an orbital period of around 570 min, observing the inner magnetosphere. The Arase satellite was launched on December 20, 2016 and started regular observations on March 23, 2017.

For the present analysis, we utilized the Low-Energy Particle Experiments-Electron Analyzer (LEP-e; Kazama et al., 2017; S.-Y. Wang et al., 2018), the Low-Energy Particle Experiments-Ion Mass Analyzer (LEP-i; Asamura et al., 2018; Asamura et al., 2018a, 2018b), the Medium-Energy Particle Experiments-Electron Analyzer (MEP-e; Kasahara et al., 2018a, 2018b; Kasahara, Yokota, Hori, et al., 2018), the Medium-Energy Particle Experiments-Ion Mass Analyzer (MEP-i; Yokota et al., 2017, 2018), the High-Frequency Analyzer (HFA; Kasahara, Kumamoto, et al., 2018; Kumamoto et al., 2018), the Onboard Frequency Analyzer (OFA; Kasahara, Kojima, et al., 2018; Matsuda et al., 2018), the spin-averaged potential data of Electric Field Detector (EFD; Kasaba et al., 2017; Kasahara, Kasaba, Matsuda, et al., 2018) of the Plasma Wave Experiment (PWE; Kasahara, Kasaba, Kojima, et al., 2018), and the Magnetic Field Experiment (MGF; Matsuoka et al., 2018a, 2018b; Matsuoka, Teramoto, Nomura, et al., 2018). For plasma particles, the Arase satellite provides plasma particle data for the energy ranges of ~ 19 – $19,000$ eV/q, 10 – 80 keV/q, ~ 10 – $25,000$ eV/q, and 10 – 180 keV/q for LEP-e, MEP-e, LEP-i, and MEP-i measurements, respectively. The PWE instruments provide magnetic-field data from 1 Hz to 100 kHz and electric-field data from DC to 10 MHz. The MGF covers the frequency ranges of EMIC waves (64 -Hz sampling data) and ultra-low-frequency (ULF) waves (8 s fitting data).

2.3. Radiation Belt Storm Probes

The RBSP mission, also known as the Van Allen Probes mission, consists of two identical satellites (RBSP-A and RBSP-B) in identical but longitudinally separated highly elliptical Earth orbits with a perigee of $\sim 7,000$ – $37,000$ km and an inclination of 10° (Kessel et al., 2013; Mauk et al., 2013). The orbital period is ~ 9 h.

Measurements of electron and ions fluxes are provided by the Helium, Oxygen, Proton and Electron (HOPE) mass spectrometer (Funsten et al., 2013), which is the low-energy instrument of the Energetic particle, Composition, and Thermal plasma (ECT) suite (Spence et al., 2013). Its energy ranges are from ~ 15 eV/q to 50 keV/q for electrons and from ~ 1 eV/q to 52 keV/q for ions (H^+ , He^+ , and O^+). The Electric and Magnetic Field Instrument and Integrated Science (EMFISIS) instrument (Kletzing et al., 2013) provides magnetic-field data at frequencies from DC to 30 Hz and electric and magnetic fields at frequencies from 10 Hz to 12 kHz (to 400 kHz for single-axis electric field).

2.4. Defense Meteorological Satellite Program

The Defense Meteorological Satellite Program (DMSP) satellites are a series of sun-synchronous polar-orbit spacecraft flying at an altitude of ~ 830 km. At all times, two or more satellites are active; F15, F16, and F18 provided the ionospheric parameters above the SAR arc on November 4, 2019. The instruments onboard the DMSP satellites include sensors to measure precipitating auroral particles (SSJ) with energies from 30 eV/q to 30 keV/q, cold/bulk plasma properties and high-resolution vertical and horizontal plasma drifts of the topside ionosphere (SSIES), the geomagnetic field (SSM; Greenspan et al., 1986; Rich & Hairston, 1994).

2.5. Global Navigation Satellite System – Total Electron Content

Two-dimensional total electron content (TEC) maps were also analyzed in the SAR-arc event on January 17, 2015. The temporal and spatial resolutions are 5 min and $0.5^\circ \times 0.5^\circ$, respectively. The TEC data were derived from collected Global Navigation Satellite System (GNSS) data in the Receiver INdependent EXchange format according to the procedure described by Shinbori et al. (2020) and Sori et al. (2019). The absolute values of vertical TEC were estimated using the technique proposed by Otsuka et al. (2002). Assuming that the ionosphere is a thin layer at an altitude of 400 km, the slant TEC were converted to vertical TEC near the geographic longitude of the Athabasca observatory. A north-south keogram of TEC was created, using the slant TEC data with a zenith angle of less than 75° .

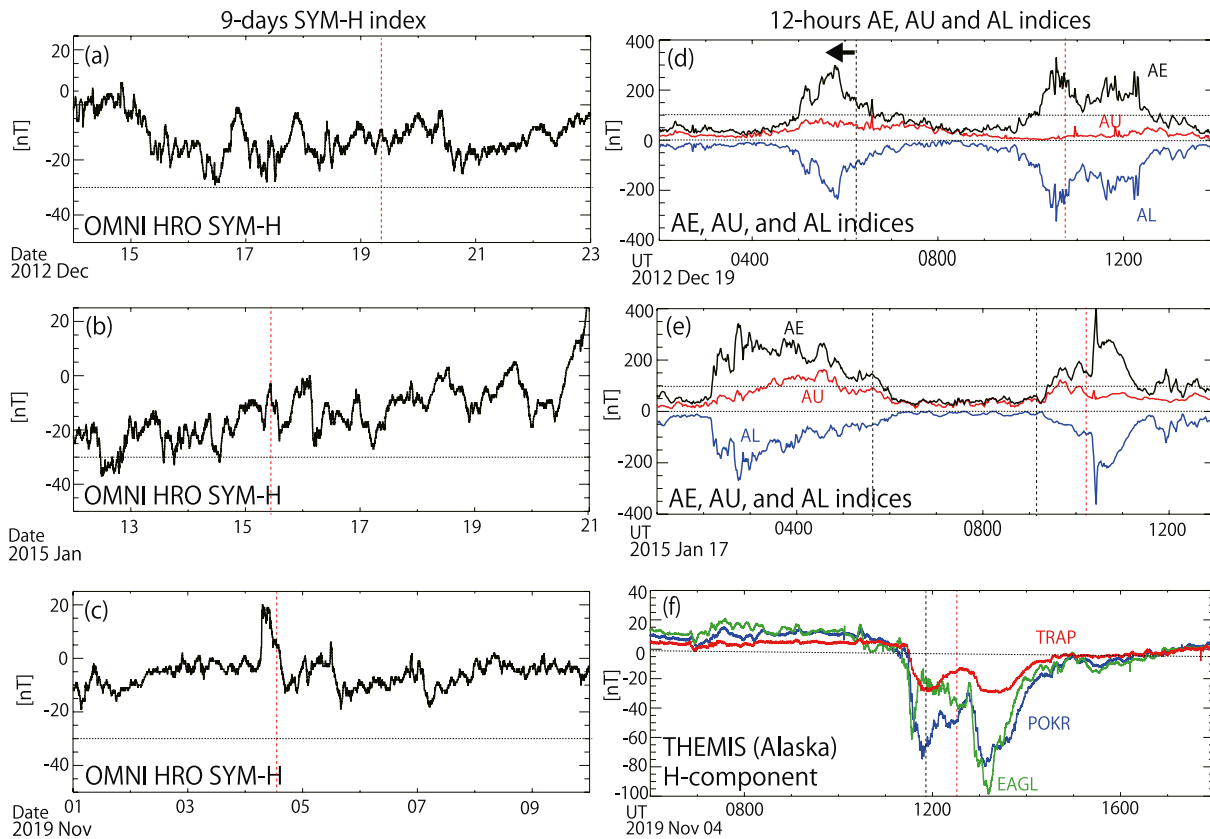


Figure 1. (a) 9-day SYM-H index on December 14–23, 2012; (b) 9-day SYM-H index on January 12–21, 2015; (c) 9-day SYM-H index on November 1–10, 2019; (d) 12-h AE, AU, and AL indices on December 19, 2012; (e) 12-h AE, AU, and AL indices on January 17, 2015; (f) H-component magnetic fields (median value subtracted) observed by ground-based magnetometer at Alaskan stations of the THEMIS project, where red, blue, and green curves are for Trapper Creek (GLAT: 62.24°N; GLON: 209.58°E), Poker Flat (GLAT: 65.12°N; GLON: 212.57°E), and Eagle (GLAT: 64.78°N; GLON: 218.83°E), respectively. The vertical black and red dashed lines show when the SAR arc emerged (black) and when Arase or RBSP crossed it (red). RBSP, Radiation Belt Storm Probes; SAR, stable auroral red; THEMIS, Time History of Events and Macroscale Interactions during Substorms.

3. Geomagnetic Activity

Figure 1 shows (left) 9 days of the SYM-H index (Iyemori, 1990; Iyemori & Rao, 1996) and (right) 12 h of the AU and AL indices (World Data Center for Geomagnetism, Kyoto et al., 2015) that include the intervals of SAR arcs on December 19, 2012 (a, d), January 17, 2015 (b, e), and November 4, 2019 (c). Because the AU and AL indices for November 4, 2019 were not published, we used the H-component magnetic-field data (median values were subtracted) at the Time History of Events and Macroscale Interactions during Substorms (THEMIS) stations at Alaska near the location of the third event in Figure 1f. The vertical black and red dashed lines in Figures 1a–1f indicate when a SAR arc emerged (black) and when Arase or RBSP crossed it (red). The arrow in Figure 1d indicates that the SAR arc emerged before the time indicated by the black dashed line (outside the observation time of the ASI). The two black dashed lines in Figure 1e indicate that the SAR arc emerged twice. The SYM-H variations indicate that each SAR arc of interest occurred during a non-storm-time substorm, defined here as those with SYM-H larger than -30 nT for the whole day but the maximum AE value greater than 100 nT. The SAR arcs analyzed in the present study emerged in association with small substorms (Figures 1d–1f). These facts suggest that the substorms are more important than geomagnetic storms for generating the SAR arcs, at least for the present events.

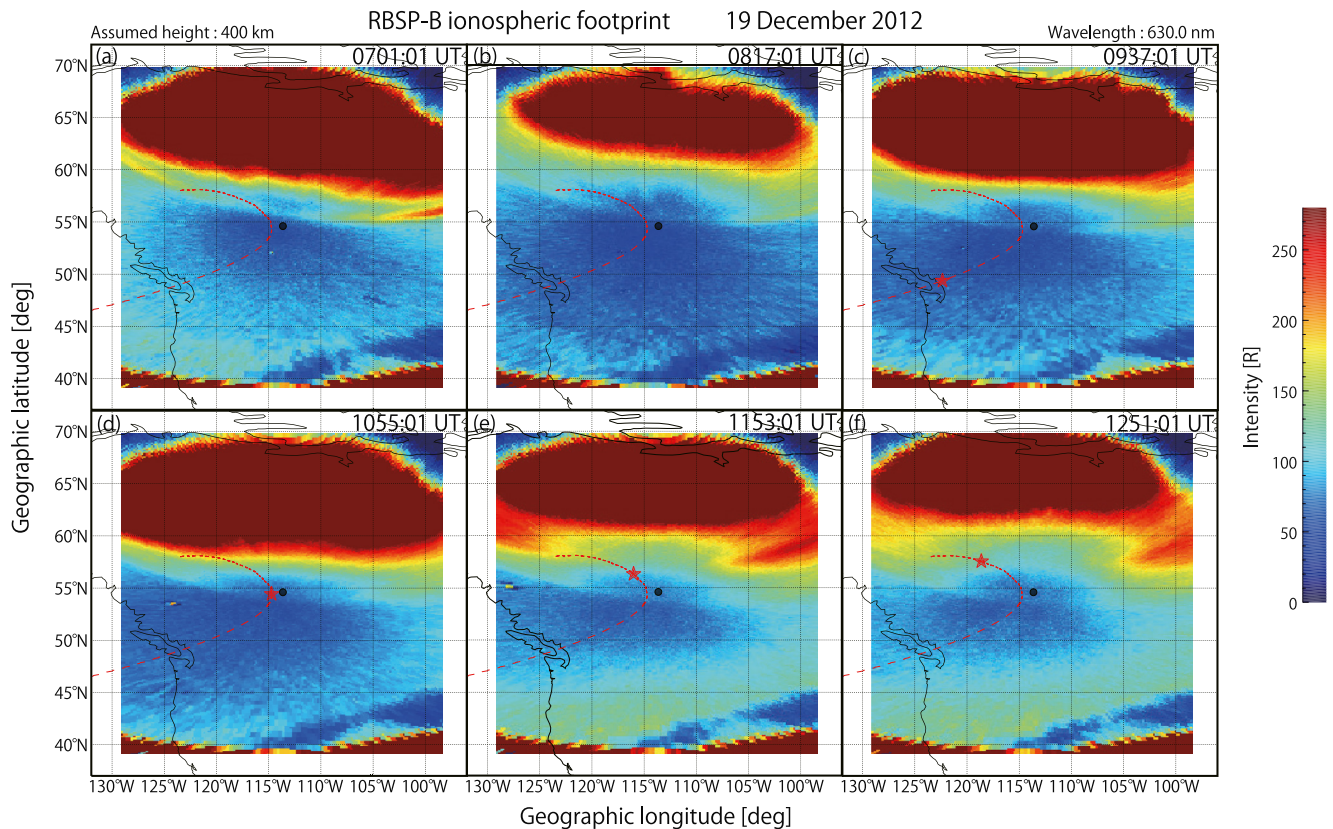


Figure 2. (a) 630-nm images captured with Athabasca all-sky imager (ASI) on December 19, 2012 at (a) 0701, (b) 0817, (c) 0937, (d) 1055, (e) 1153, and (f) 1251 UT. These images were converted to geographic coordinates by assuming 630-nm emission altitude of 400 km. The red dashed curves show the trajectory of the footprint of the RBSP-B satellite mapped at an altitude of 400 km using the TS05 model. The red stars indicate the positions of the RBSP-B footprint when the images were taken. The horizontal and vertical axes correspond to geographic longitude and latitude, respectively. The black dot at the center of each image indicates the location of the Athabasca station. RBSP, Radiation Belt Storm Probes.

4. Event 1: Weak SAR-Arc Event on December 19, 2012

4.1. Ground-Based Observations

Figure 2 shows 630.0-nm airglow/auroral images taken at 0701–1251 UT on December 19, 2012 at Athabasca. Raw images were mapped to geographical coordinates by assuming that the altitude of the 630-nm emission is 400 km. The saturated region in the northern half of the images corresponds to the main auroral oval. A SAR arc emerged at subauroral latitudes from ~0611 UT when the observation started, then its emission intensity gradually decreased. The red dashed curves show the ionospheric footprint trajectory of RBSP-B traced to an altitude of 400 km using the Tsyganenko-Sitnov 05 (TS05) geomagnetic-field model (Tsyganenko & Sitnov, 2005). Based on Figure 2d, the RBSP-B satellite crossed the faint SAR arc at ~1055 UT. The brightness of the faint SAR arc at the time of crossing is ~65 R. Movie S1 provides a more detailed view of the spatiotemporal variations of the emerged SAR arc during 0611–1407 UT.

Figure 3a and 3b show north-south keograms for 557.7 and 630.0-nm images assuming emission altitudes of 120 and 400 km, respectively. These keograms indicate the temporal variation of emission intensity at the longitude of the Athabasca station (246.36°E). Figure 3b shows that the SAR emerged slightly equatorward of the southward edge of the main auroral oval (~56°N) at ~0600 UT when the observation began, and the SAR-arc emission lasted for more than 7 h with varying intensity until 1330 UT, judging from the SAR-arc position indicated by the pink arrows. In the 557.7-nm keogram of Figure 3a, a belt-like emission region appears at geographic latitudes at 50°–53°N throughout the plotted interval (~0600–1410 UT). The belt-like emission is not real auroral/airglow emission, but probably due to the reflection of the strong auroral emission in the northern sky by the dome. (Note that this reflection is also seen in keograms of events 2 and 3).

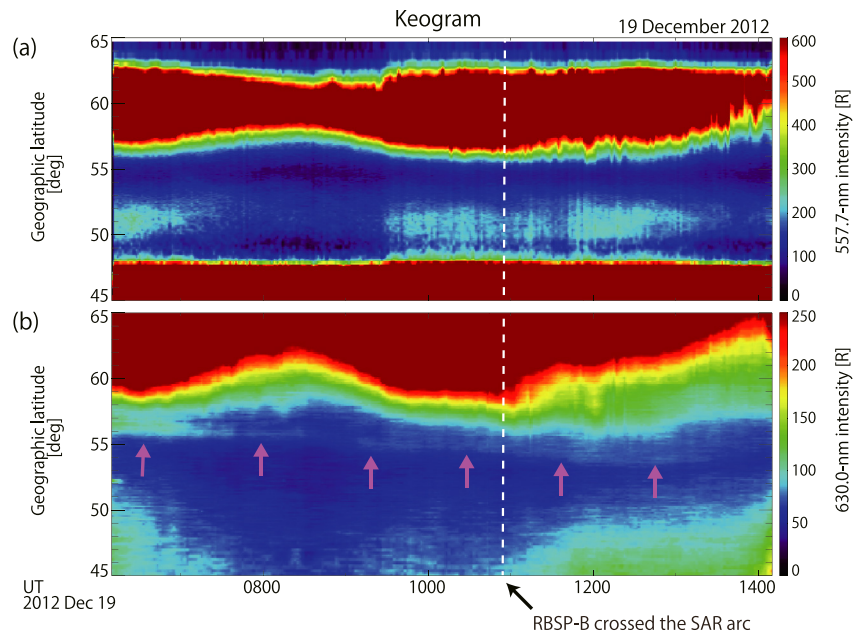


Figure 3. (a) Keograms obtained by slicing (a) 557.7-nm and (b) 630.0-nm images at the Athabasca station in meridional direction from ~0600 to 1410 UT on December 19, 2012. The pink arrows in (b) indicate the location of the SAR arc. The vertical white dashed line shows when RBSP-B crossed the SAR arc. RBSP, Radiation Belt Storm Probes; SAR, stable auroral red.

Besides it, there is no 557.7-nm emission at the position of the 630-nm arc. Based on these observations, we judged that the observed 630-nm arc was a SAR arc.

4.2. RBSP-B Observations

Magnetospheric source observations by the RBSP-B satellite are shown in Figures 4 and 5. Figure 4 shows the observations of plasma particles used to investigate the mechanism of SAR-arc generation by Coulomb collisions, namely (a) the electron density calculated from the upper frequency limit of upper hybrid resonance (UHR) waves observed by RBSP-B/EMFISIS and (b) the omnidirectional H^+ flux, (c) the omnidirectional He^+ flux, and (d) the omnidirectional O^+ flux, all observed by RBSP-B/HOPE. Figures 4e–4g show the heat fluxes estimated from Coulomb collisions of H^+ , He^+ , and O^+ , respectively, with ambient electrons. Figure 4h shows the total electron heat fluxes. The heat flux due to Coulomb collisions was estimated from the ion flux observed by RBSP-A/HOPE and the electron density in Figure 4a observed by RBSP-B/EMFISIS with the same methods as those used by Jordanova et al. (1996) and Kozyra et al. (1987). The ion flux data used for the heat-flux calculation cover an energy range from ~102 eV/q to ~52 keV/q. This energy range was divided into 59 bins in a logarithmic scale. We assume for all three events that the composition of the plasmaspheric plasma was $H^+:He^+:O^+ = 77:20:3$ with a temperature of 1 eV. Figure 4i shows the omnidirectional electron fluxes observed by RBSP-B/HOPE. The black vertical dashed line indicates when RBSP-B crossed the SAR arc, as determined from the 630-nm intensity variation in Figure 4j. McIlwain's L-parameter (L_m ; McIlwain, 1961), magnetic local time (MLT), MLAT, radial distance (R), and the universal time (UT) of RBSP-B are shown below the horizontal axis; these parameters were derived using the TS05 model.

In this event, RBSP-B crossed the plasmapause at ~1100 UT, as shown in Figure 4a. Based on Figures 4b–4d, the fluxes of the ring-current ions with an energy range of ~101 eV/q–51.7 keV/q were observed. As shown in Figures 4e–4g, the heat flux from the H^+ flux to the ambient cold electrons was one order of magnitude larger than those of He^+ and O^+ . The total heat flux reached $\sim 2.5 \times 10^9$ eV/cm²/s above the emerged SAR arc. Figure 4i indicates that the SAR arc occurred near the inner edge of the electron plasma sheet.

The electromagnetic-field variations observed by RBSP-B are shown in Figure 5, based on which we investigate EMIC waves and KAWs as SAR-arc generation mechanisms. Figures 5a–5c show dynamic wavelet

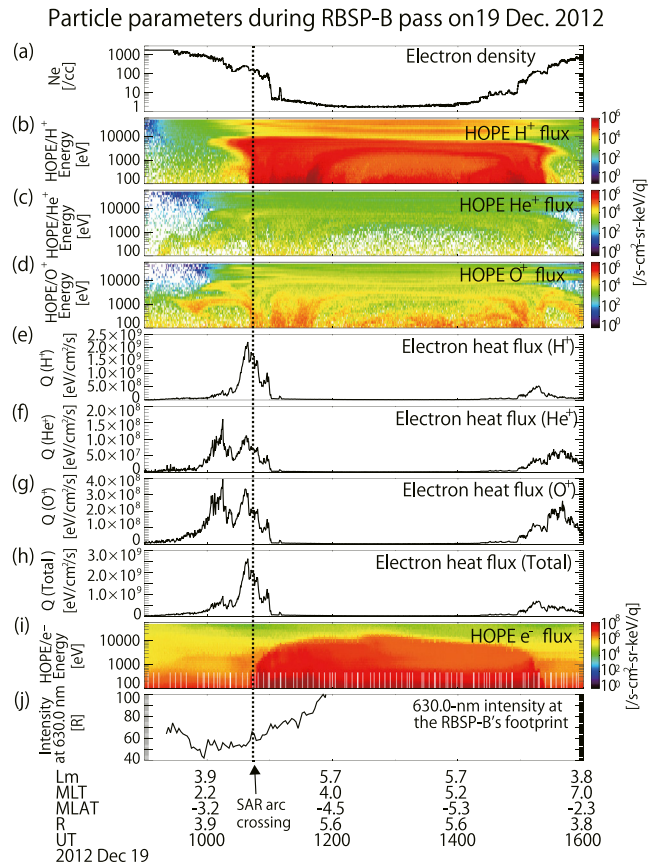


Figure 4. From top to bottom: (a) electron density calculated from upper hybrid resonance (UHR) frequency; (b) omnidirectional H^+ flux; (c) omnidirectional He^+ flux; (d) omnidirectional O^+ flux; estimated heat flux due to Coulomb collisions between electrons and (e) H^+ , (f) He^+ , and (g) O^+ ; (h) total heat flux; (i) 630.0-nm airglow/auroral intensities observed at Athabasca in RBSP-B footprint. The vertical dashed line shows when RBSP-B crossed the SAR-arc peak. RBSP, Radiation Belt Storm Probes; SAR, stable auroral red.

Based on Figures 4e–4g, the heat flux from the H^+ to ambient cold electrons was one order of magnitude larger than those for He^+ and O^+ , indicating that H^+ is most important for this SAR-arc generation. From Figure 4h, the total heat flux reached $\sim 2.5 \times 10^9$ eV/cm²/s above the SAR arc. According to the calculation by Kozyra et al. (1993, 1997), the generation of a SAR arc with an emission intensity of ~ 65 R observed in this study (Figure 4j) would require an electron heat flux of $\sim 8.0 \times 10^9$ eV/cm²/s in winter during solar maximum. This value is comparable to that estimated ($\sim 2.5 \times 10^9$ eV/cm²/s) based on the present observation. Thus, we conclude that this SAR arc was probably caused by the heat flux flowing from the magnetosphere through Coulomb collisions between the observed ring-current ions and plasmaspheric electrons/ions. The difference in latitudinal width between the heat flux and the SAR arc in Figure 4 may have been because the SAR arc was embedded in the background 630-nm airglow emission (~ 50 R as identified from Figures 2 and 4j) and thus should be identified only around the peak of the SAR-arc emission.

5. Event 2: Plasmapause Skimming Event on January 7, 2015

5.1. Ground-Based Observations

Figure 6 shows the 630.0-nm airglow/auroral images taken at 0641–1047 UT on January 17, 2015 at Athabasca, converted to geographical coordinates by assuming a 630-nm emission altitude of 400 km. The

spectra of the magnetic-field variations observed by RBSP-B/EMFISIS (4-s fitting data) at frequencies of 1–125 mHz to examine KAWs. The three magnetic-field components in solar magnetic (SM) coordinates are shown in Figures 5a–5c. The red vertical dashed line indicates when the RBSP-B satellite crossed the SAR arc as identified from the 630-nm intensity in Figure 5g. Lanzerotti et al. (1978) reported ~ 8.3 - and ~ 9.5 -mHz hydromagnetic waves observed on the ground simultaneously with SAR arcs, but Figures 5a–5c show no increase in power spectral density (PSD) associated with the SAR arc.

In Figures 5d–5f, we evaluate the mechanism for SAR-arc generation by EMIC waves. These figures show dynamic spectra of the magnetic field observed by EMFISIS (64-Hz data) at frequencies of 0.1–30 Hz. The three magnetic-field components in SM coordinates are shown in Figures 5d–5f. The cyclotron frequencies of H^+ , He^+ , and O^+ are plotted on these panels. There is no enhancement of PSD associated with the SAR arc. According to Anderson et al. (1992a, 1992b), the average PSD of EMIC waves is ~ 5.0 nT²/Hz in the magnetosphere. However, the observed PSD in this frequency range is $\sim 5.0 \times 10^{-3}$ nT²/Hz at a maximum, which is too weak to identify any EMIC waves in the SAR-arc source. Figures 5d–5f show horizontal band enhancements of PSD at fixed frequencies of ~ 0.1 – 0.2 Hz at all times; these band enhancements are considered to be artificial noise because their frequencies are almost constant.

4.3. Discussion

First, we discuss the generation mechanism of SAR arcs due to electromagnetic waves based on Figures 5a–5f. As shown in Section 4.2, in Figures 5d–5f there is no increase of PSD associated with the SAR arc. At frequencies of ~ 10 mHz, the PSD is at most ~ 1 nT²/Hz. On the basis of Figures 5d–5f, there was no PSD enhancement at frequencies of ~ 0.1 – 32 Hz. This fact suggests that EMIC waves or 0.1–32-Hz electromagnetic waves did not contribute to the generation of the SAR arc for this event.

Second, we consider the generation mechanism of SAR arcs by Coulomb collisions. Clearly, the SAR arc was in the overlap region of ring-current ions (Figures 4b–4d) and the plasmasphere (Figure 4a), although the latitudinal width of the SAR arc was smaller than that of the overlap region.

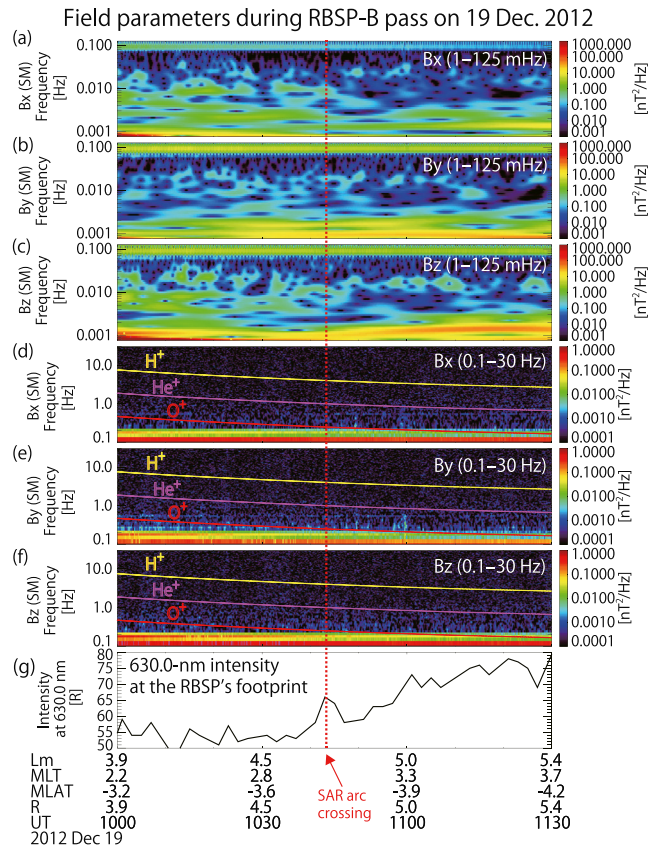


Figure 5. From top to bottom: (a–c) wavelet spectra of magnetic field at frequencies of 1–125 mHz observed by ECT onboard RBSP-B; (d–f) fast-Fourier-transform spectra of magnetic field at frequencies of 0.1–30 Hz (the yellow, pink, and red curves represent the gyro frequencies of H^+ , He^+ , and O^+ , respectively, at the satellite's position); (g) 630.0-nm airglow/auroral intensities observed at Athabasca in RBSP-B footprint. The red vertical dashed line shows when RBSP-B crossed the SAR-arc peak. ECT, Energetic particle, Composition, and Thermal plasma; RBSP, Radiation Belt Storm Probes; SAR, stable auroral red.

observed by RBSP-A/HOPE. Figures 8e–8g show the heat fluxes estimated by considering Coulomb collisions of H^+ , He^+ , and O^+ , respectively, with ambient electrons. The heat fluxes due to Coulomb collisions were estimated from the ion flux observed by RBSP-A/HOPE and the electron density in Figure 8a observed by RBSP-A/EMFISIS with the same methods as in event 1. The ion flux used for the heat-flux calculation has an energy range from ~ 98 eV/q to ~ 52 keV/q. This energy range was divided into 42 bins in a logarithmic scale. Figure 8h shows the total electron heat fluxes, Figure 8i shows the omnidirectional electron flux observed by RBSP-A/HOPE, and Figure 8j shows the 630.0-nm airglow/auroral intensity at the RBSP-A footprint location at an altitude of 400 km.

In the present event, RBSP-A was skimming the plasmopause, as shown in Figure 8a. The sharp increases and decreases in electron density (e.g., at 0500 and 0630–0720 UT) observed in Figure 8a are considered to have been caused by relative motion of RBSP-A entering and exiting the plasmasphere. As shown in Figures 8b–8d, the fluxes of the ring-current ions with energies of ~ 0.1 –20 keV/q were observed. In Figures 8e–8g, the heat flux from energetic H^+ to the ambient cold electrons was one order of magnitude higher than that of He^+ and more than twice as high as that of O^+ . The total heat flux reached $\sim 5.0 \times 10^9$ eV/cm²/s above the emerged SAR arc. However, the total heat flux at ~ 0600 UT – when RBSP-A was located at subauroral latitudes but did not cross the SAR arc – was higher than that at ~ 1000 UT when RBSP-A crossed the SAR arc. Figure 8i indicates that the SAR arc occurred near the inner edge of the electron plasma sheet.

saturated region in the northern half of each image corresponds to the main auroral oval. The SAR arc emerged at subauroral latitudes at ~ 0900 UT as shown in Figure 6c. Subsequently, the emission intensity gradually increased. The red dashed curves indicate the ionospheric footprint trajectory of RBSP-A traced to an altitude of 400 km using the TS05 model. Figures 6a–6f show that RBSP-A was located at subauroral latitudes for a long time from ~ 0640 to ~ 1050 UT. Figure 6d and 6e indicate that RBSP-A passed over the emerged SAR arc at ~ 0940 –1010 UT. The brightness of the SAR arc at the time of crossing is ~ 110 R. Movie S2 provides a more detailed view of the spatiotemporal variations of the emerged SAR arc during 0111–1237 UT.

Figure 7a shows a north-south keogram of TEC at the geographic longitude of the Athabasca station (246.36° E). A clear TEC depletion (< 3.0 TECU) with a latitudinally narrow structure was observed at latitudes of 48° – 55° from ~ 0900 UT, indicating the deep ionospheric trough. Figure 7b and 7c show north-south keograms for 557.7- and 630.0-nm images assuming the emission heights of 120 and 400 km, respectively. These keograms indicate the temporal variation of emission intensity at the longitude of the Athabasca station. Figure 7b shows that the SAR arc emerged slightly equatorward of the southward edge of the main auroral oval ($\sim 55^\circ$ N) at ~ 0940 UT, and the SAR-arc emission lasted until 1240 UT (judging from the SAR-arc position indicated by the pink arrows), when the observation ended. In Figure 7c, 557.7-nm emission corresponding to the 630-nm SAR arc does not appear in the 557.7 nm keogram. Thus, we identify that the observed 630-nm arc is a SAR arc. Additionally, this SAR arc appeared near the poleward edge of the deep ionospheric trough shown in Figure 7a.

5.2. RBSP-A Observations

The magnetospheric source observations by the RBSP-A satellite are shown in Figures 8 and 9. Figure 8 shows the observations of plasma particles relevant to the SAR-arc generation mechanism by Coulomb collisions. Figure 8 shows (a) the electron density calculated from the upper frequency limit of UHR waves, (b) the omnidirectional H^+ flux, (c) the omnidirectional He^+ flux, and (d) the omnidirectional O^+ flux, all ob-

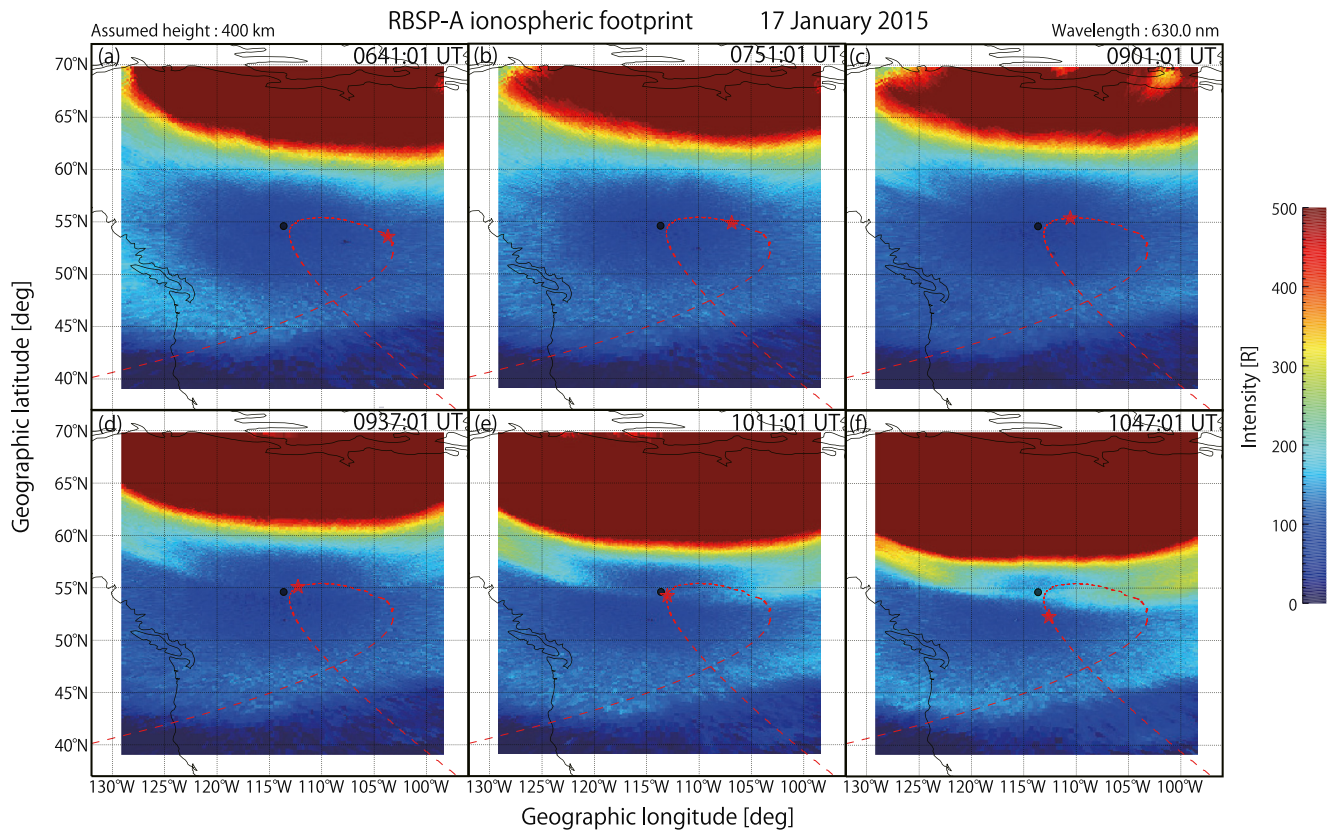


Figure 6. 630-nm images captured with Athabasca ASI on January 17, 2015 at (a) 0641, (b) 0751, (c) 0901, (d) 0937, (e) 1011, and (f) 1047 UT. These images were converted to geographic coordinates by assuming 630-nm altitude of 400 km. The red dashed curves show the trajectory of the footprint of the RBSP-A satellite mapped at an altitude of 400 km using the TS05 model. The red stars indicate the positions of the footprint of RBSP-A when the images were taken. The horizontal and vertical axes correspond to the geographic longitude and latitude, respectively. The black dot at the center of each image indicates the location of the Athabasca station. ASI, all-sky imager; RBSP, Radiation Belt Storm Probes.

Figure 9 shows the electromagnetic-field variations observed by RBSP-A. Figures 9a–9c show dynamic wavelet spectra of the magnetic-field variations observed by RBSP-A/EMFISIS (4-s fitting data) at frequencies of ~1–125 mHz to evaluate KAWs. The three magnetic-field components in SM coordinates are shown. Based on Figures 9a–9c, the PSD was enhanced at frequencies of 7–20 mHz at ~1015 UT as indicated by pink arrows, but only above the SAR arc. Figure 9d shows the SM-coordinate magnetic-field deviation from the 500-s running averages. This figure indicates that the 7–20-mHz electromagnetic waves at ~1015 UT had a wave amplitude of ~0.9 nT (peak to peak) in the B_z component.

Figures 9e–9g show dynamic spectra of the magnetic field observed by RBSP-A/EMFISIS (64-Hz data) at frequencies of 0.1–30 Hz. The three magnetic-field components in SM coordinates are shown. The cyclotron frequencies of H^+ , He^+ , and O^+ are displayed in these panels as a reference to examine possible EMIC wave activity. However, neither EMIC nor any other waves associated with the SAR arc were not observed.

5.3. Discussion

First, we consider the SAR-arc generation mechanism in terms of electromagnetic waves. As discussed in Section 5.2, the enhancement in PSD at frequencies of 7–20 mHz at ~1015 UT was possibly related to the SAR arc having KAWs as the generation mechanism. The amplitude of the 7–20-mHz ULF waves was at most 0.9 nT (peak to peak), as shown in Figure 9d. Lanzerotti et al. (1978) concluded that a wave amplitude of 10 nT was necessary to generate the SAR arc that they analyzed. Their work may indicate that the observed 7–20 mHz waves were perhaps too weak to cause the SAR arc in the present study. These enhancements of PSD at frequencies of 7–20 mHz may coincide with the onset of a small substorm at ~1015 UT, as

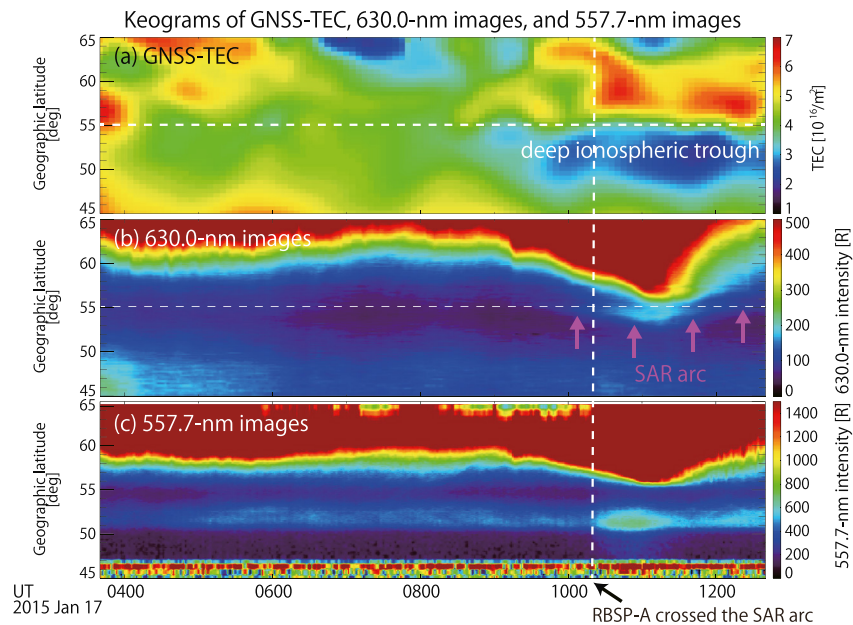


Figure 7. (a) Keogram of total electron content (TEC) map at longitude of the Athabasca station (246.36°E), and keograms obtained by north-south slicing the (b) 630.0 nm and (c) 557.7 nm images at the longitude of Athabasca, from 0340 to 1240 UT on January 17, 2015. The pink arrows in (b) indicate the location of the SAR arc. The vertical white dashed line shows when RBSP-A crossed the SAR arc. The two horizontal white dashed lines in Figure 7a and 7b show the poleward boundary of the SAR arc. RBSP, Radiation Belt Storm Probes; SAR, stable auroral red.

shown in the AU and AL indices of Figure 1e. It has been reported by many studies that Pi2 pulsations occur in the ULF band with a period range from 40 to 150 s at the onset of substorms (or auroral intensifications; e.g., Liou et al., 2000). The observed ULF waves last for ~30 min, indicating that the duration is too long for Pi2 pulsations associated with onset, and may instead suggest that this low-amplitude ULF wave is associated with the SAR arc. On the basis of Figures 9e–9g, there was no enhancement of PSD at frequencies of ~0.1–32 Hz, indicating that 0.1–32-Hz electromagnetic waves did not contribute to the generation of the SAR arc for this event.

Second, we consider the SAR-arc generation mechanism due to Coulomb collisions. Based on Figures 9e–9g, the heat flux from the H^+ flux to the ambient cold electrons was one order of magnitude higher than that of He^+ and more than twice as high as that of O^+ , indicating that H^+ is most important for this SAR-arc generation. As shown in Figure 8h, the total heat flux reached $\sim 5.0 \times 10^9$ eV/cm²/s above the emerged SAR arc. Kozyra et al. (1993, 1997) suggested that the generation of a SAR arc with an emission intensity of 110 R as observed herein (Figure 9h) would require an electron heat flux of $\sim 9.0 \times 10^9$ eV/cm²/s in winter during solar maximum, which is comparable to the estimated one ($\sim 5.0 \times 10^9$ eV/cm²/s) based on the present observation.

We should discuss the fact that the total heat flux at ~0600 UT, when RBSP-A did not cross the SAR arc, was larger than that at ~1015 UT, when it did cross. We consider here the density variation of the ionospheric plasma as the receptor condition of heat flux. In previous studies, SAR arcs were observed either at the minimum of the ionospheric trough (e.g., Inaba et al., 2020; Mendillo et al., 2016) or on the equator edge of the trough (e.g., Kozyra et al., 1997). If the heat flux is supplied to the region with low plasma density (i.e., trough), then each electron can receive more heat without ion cooling effects, and the electron temperature (T_e) tends to increase (e.g., Kozyra et al., 1997; Prölss, 2006). Although Figures 7a and 7b actually show that the SAR arc emerged near the poleward edge of the deep ionospheric trough, no such trough was observed by RBSP-A at ~0600 UT when the heat flux increased. This could be why the SAR arc emerged only at ~1015 UT when the background plasma density in the ionosphere was small. The other possibility is that, according to the 630-nm continuous images in Movie S2, the SAR arc appeared slightly north of the RBSP-B footprint at ~0600 UT, suggesting a possible error in the field-line mapping of the satellite position. In other

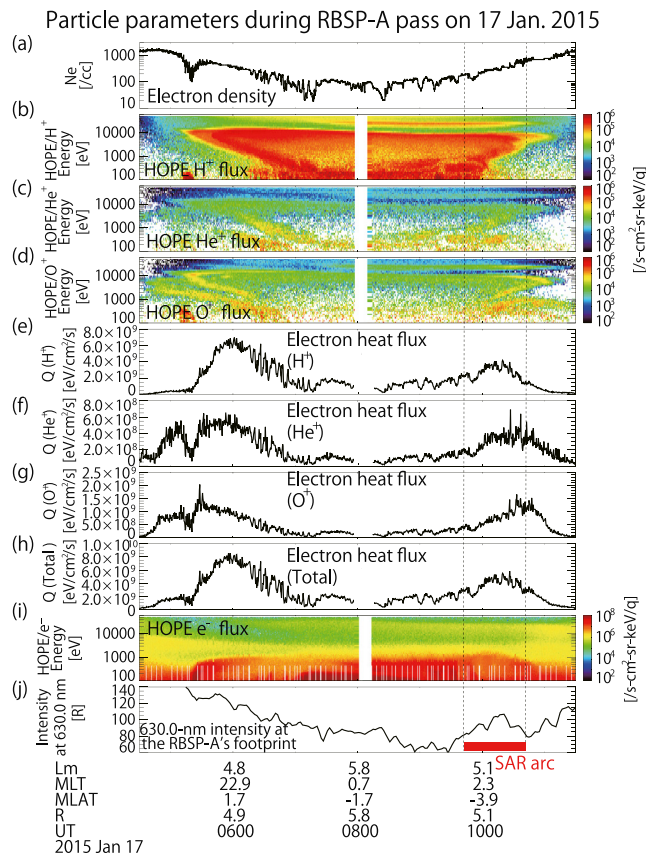


Figure 8. From top to bottom: (a) electron density; (b) omnidirectional H^+ flux; (c) omnidirectional He^+ flux; (d) omnidirectional O^+ flux; estimated heat flux due to Coulomb collisions between electrons and (e) H^+ , (f) He^+ , and (g) O^+ ; (h) total heat flux; (i) omnidirectional electron flux (all observed by RBSP-A satellite); (j) 630.0-nm airglow/auroral intensities observed at Athabasca in RBSP-A footprint. RBSP, Radiation Belt Storm Probes.

observations support the idea that the 630-nm arc was a SAR arc. However, only around the time at which the arc detached (i.e., ~ 1200 UT), a string-like region of 557.7 nm extending in the east-west direction appeared in the eastern part of the images, as shown in the sequential 557.7-nm images in Movie S4. We find no such string-like structure in the keogram of Figure 11a, which contains only latitudinal information around the image center. SAR arcs with weak green-line emission have been reported by past studies (e.g., Mendillo et al., 2016), but the green-line emission in the present event was brighter.

6.2. Arase Observations

The observations of the magnetospheric source by the Arase satellite are shown in Figures 12 and 13. Figure 12 shows plasma-particle observations for investigating SAR-arc generation due to Coulomb collisions. Figure 12 shows (a) the electron density calculated from the upper frequency limit of UHR waves (solid curve) and the satellite potential (dashed curve), and the omnidirectional (b) H^+ , (c) He^+ , (d) O^+ , and (e) electron fluxes, all observed by the Arase satellite. Figures 12f–12h show the heat fluxes estimated by considering Coulomb collisions of H^+ , He^+ , and O^+ , respectively, with ambient electrons. The heat fluxes due to Coulomb collisions were estimated from the ion flux observed by Arase/LEP-i and MEP-i and the electron density based on the UHR frequency observed by Arase/PWE with the same methods as in events 1 and 2.

The ion flux data used for the heat-flux calculation have energy ranges from ~ 114 eV/q to ~ 25.5 keV/q for LEP-i and from ~ 27.3 to ~ 97.3 keV/q for MEP-i. These energy ranges were divided into 20 bins and 7

words, the enhancement of the heat flux at 0600 UT may correspond to the SAR-arc emission occurring at a slightly higher latitude ($\sim 55^\circ N$) than that of the RBSP-B footprint ($\sim 52.5^\circ N$) at ~ 0600 UT. However, even in this case, although the emission intensity at ~ 1015 UT was larger than that at 0600 UT, the heat flux was smaller. Again, there is a discrepancy between the heat flux and the emission intensity, suggesting the importance of other factors such as ionospheric density, the receptor condition of heat flux.

6. Event 3: Freshly Detached Bright SAR-Arc Event on November 4, 2019

6.1. Ground-Based Observations

Figure 10 shows the 630.0-nm airglow/auroral images taken at 1132–1455 UT on November 4, 2019 at the Gakona station. These images were converted to geographical coordinates by assuming an emission altitude of 400 km. The saturation in the northern half of each image in Figure 10 corresponds to the main auroral oval. The SAR arc detached from the auroral oval at ~ 1158 UT and then moved equatorward and its emission intensity gradually weakened. The red dashed curves represent the ionospheric footprint of the Arase satellite traced to an altitude of 400 km using the TS05 model. On the basis of Figure 10c, the Arase satellite crossed the freshly detached bright SAR arc at ~ 1215 UT. The brightness of the freshly detached SAR arc at the time of crossing is ~ 1.5 kR. Movie S3 provides a detailed view of the spatiotemporal variations of the SAR arc during 0900–1526 UT.

Figures 11a and 11b show north-south keograms for 557.7- and 630.0-nm images along the meridian over the Gakona station, assuming emission heights of 120 and 400 km, respectively. Figure 11b indicates that the SAR arc detached from the southward edge of the auroral oval ($\sim 62^\circ N$) at ~ 1200 UT, and the SAR-arc emission lasted until ~ 1530 UT (judging from the SAR-arc position indicated by the pink arrows), when the observation ended. By contrast, no such detached structure emerged from the auroral oval in the 557.7-nm keogram shown in Figure 11a. These observations

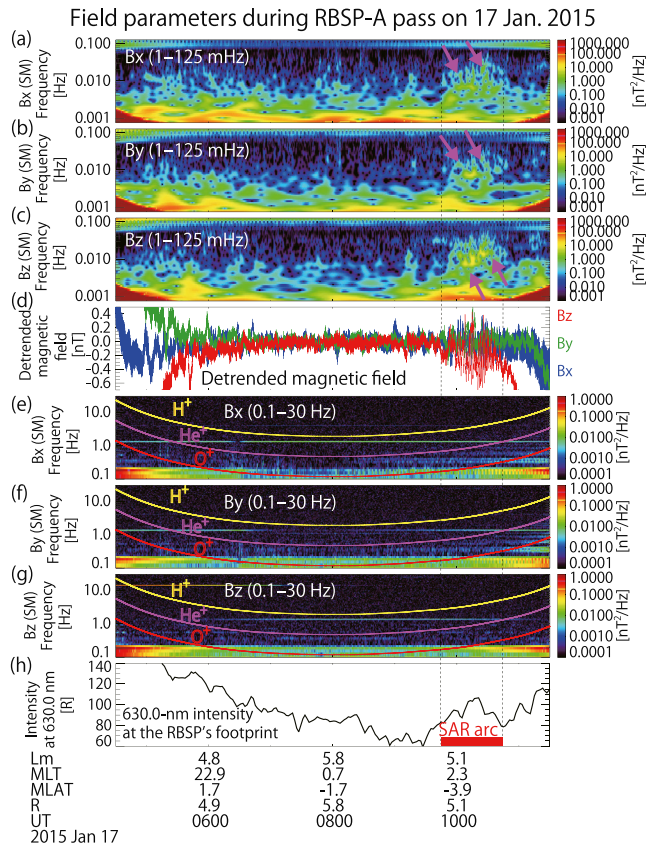


Figure 9. From top to bottom: (a–c) wavelet spectra of magnetic field at frequencies of 1–125 mHz observed by ECT onboard RBSP-B; (d) magnetic-field deviation from 500-s running averages; (e–g) fast-Fourier-transform spectra of magnetic field at frequencies of 0.1–30 Hz (the yellow, pink, and red curves represent the gyro frequencies of H^+ , He^+ , and O^+ , respectively, at the satellite's position); (h) 630.0-nm airglow/auroral intensity observed at Athabasca in the RBSP-A footprint. Pink arrows indicate PSD enhancements at frequencies of 7–20 mHz. ECT, Energetic particle, Composition, and Thermal plasma; PSD, power spectral density; RBSP, Radiation Belt Storm Probes.

bins in a logarithmic scale for LEP-i and MEP-i data, respectively. Figure 12i shows the total electron heat flux, and Figures 12j and 12k show the 630.0- and 557.7-nm airglow/auroral intensities, respectively, at the pixels of the Arase footprint at a height of 400 km. The blue dashed curve in Figure 12j shows the 630-nm emission intensity at the Arase footprint traced to an altitude of 300 km using the TS05 model.

The freshly detached SAR arc was observed with the locally intensified 557.7-nm emission and was mapped to the plasmopause-ring-current interaction region, as shown in Figures 12a and 12b. The observed freshly detached arc was not a standard SAR arc because it was not pure red. As shown in Figures 12b, 12c, and 12e, enhancements of the H^+ , He^+ , and electron fluxes (<1 keV/q) were observed near the freshly detached bright SAR arc. In Figures 12f–12h, the heat flux from the H^+ flux to the ambient cold electrons was one order of magnitude higher than those of He^+ and O^+ . As shown in Figure 12i, the estimated total electron heat flux reached 4×10^8 eV/cm²/s. Kozyra et al. (1993, 1997) suggested that the emission intensity of a SAR arc should be 10^0 – 10^1 R at solar minimum (year 2015) if the electron heat flux from the source region is $\sim 2 \times 10^8$ eV/cm²/s. The estimated heat flux for the present event seems to be too weak to cause the observed 1.5-kR red arc. We reason that the freshly detached arc corresponds to the local enhancement of low-energy electron fluxes at energies below ~ 1 keV/q at 1157–1207 UT in Figure 12e. The difference between the location of the freshly detached SAR arc (Figures 12i and 12j) and the local increases in electron fluxes (Figure 12e) is due to the field-line mapping error; this point is further discussed in Section 6.4. Note also that this local enhancement of electron flux at energies below ~ 1 keV/q was observed with a similar local enhancement of ion fluxes at energies below ~ 1 keV/q in Figure 12b. These flux enhancements occurred immediately after the peak of the total electron heat flux shown in Figure 12i.

Figures 13a–13j show the electromagnetic-field variations observed by Arase. Figure 13k shows the pitch-angle distribution of the LEP-e low-energy electron flux at energies of 0.1–1.0 keV/q. Figure 13a shows the electric-field spectra from 10 kHz to 3 MHz observed by Arase/HFA; the white dotted curve indicates the UHR frequency, indicating a clear plasmopause crossing at ~ 1200 UT. Figures 13b and 13c show the electric-field and magnetic-field spectra from 10 Hz to 20 kHz observed by

Arase/OFA; the white curves indicate the local electron cyclotron frequency (f_{ce}), $2f_{ce}$, $0.5f_{ce}$, and $0.1f_{ce}$. In Figures 13a–13c, the signals appearing at all frequencies at ~ 1200 – 1210 UT were caused by calibration. Figures 13b and 13c show the PSD enhancements at frequencies of ~ 1 kHz (0.1 – $0.5f_{ce}$) collocated with the local flux enhancements of electrons in Figures 13k and 13m, suggesting that lower-band chorus (LBC) waves were associated with the freshly detached SAR arc. Figure 13b shows that electrostatic electron cyclotron harmonic (ECH) waves were observed at 1155–1230 UT, as shown by the pink rectangle.

Figures 13d–13f show dynamic wavelet spectra of the magnetic-field variations observed by Arase/MGF (8-s fitting data) at frequencies of 1–62.5 mHz to examine KAWs. Figure 13g shows the magnetic perturbations obtained by subtracting the International Geomagnetic Reference Field (IGRF)-13 model (e.g., Thébaud et al., 2015; time resolution: 8 s). The three magnetic-field components in SM coordinates are shown. In Figures 13d–13f, there are increases in PSD (especially in the Z component) at frequencies of 7–10 mHz at ~ 1150 – 1210 UT, which is close to the location of the electron flux enhancement. Figure 13g shows a local B_z decrease at ~ 1200 UT. The PSDs at 4–10 mHz were observed continuously at 1130–1400 UT irrespective of the SAR arc.

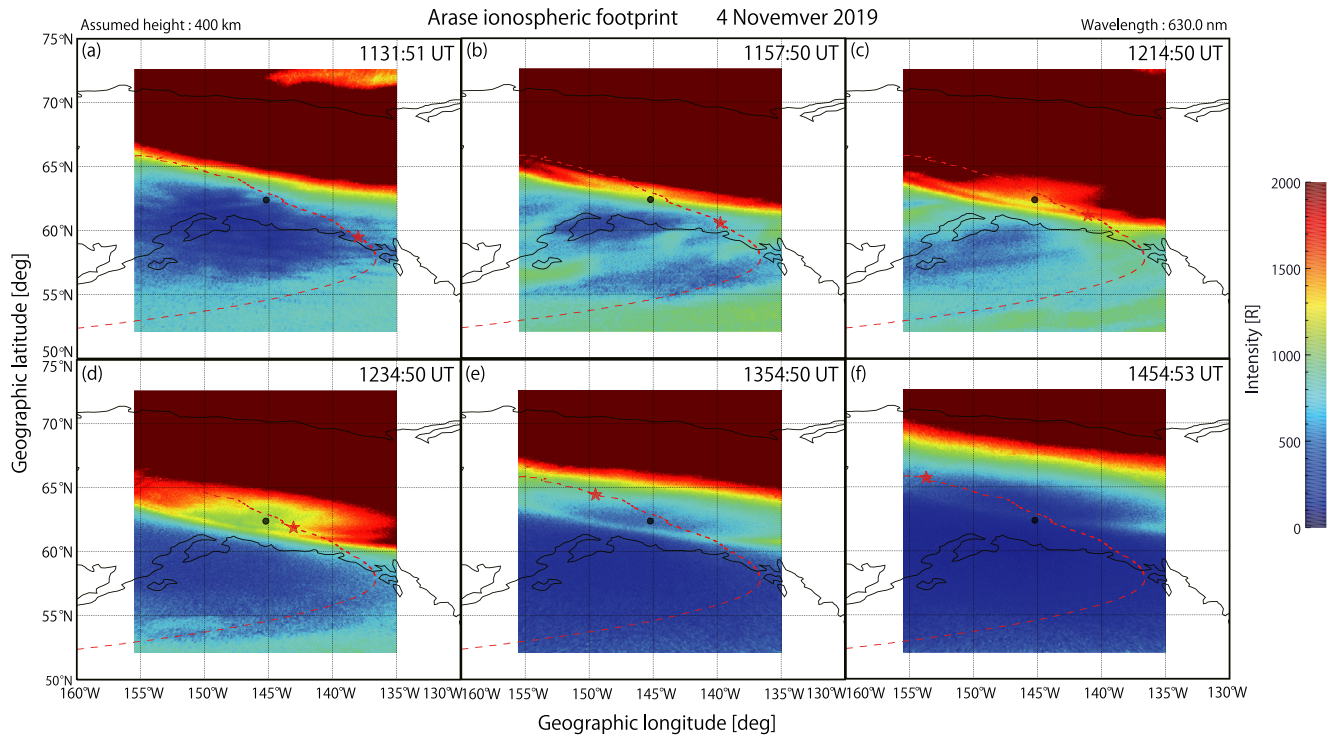


Figure 10. (a) 630-nm images captured with Gakona ASI on November 4, 2019 at (a) 1132, (b) 1158, (c) 1215, (d) 1235, (e) 1355, and (f) 1455 UT. These images were converted to geographic coordinates by assuming 630-nm emission altitude of 400 km. The red dashed curves show the trajectory of the footprint of the Arase satellite mapped at an altitude of 400 km using the TS05 model. The red stars indicate the positions of the footprint of Arase when the images were taken. The horizontal and vertical axes correspond to the geographic longitude and latitude, respectively. The black dot at the center of each image indicates the location of the Gakona station. ASI, all-sky imager.

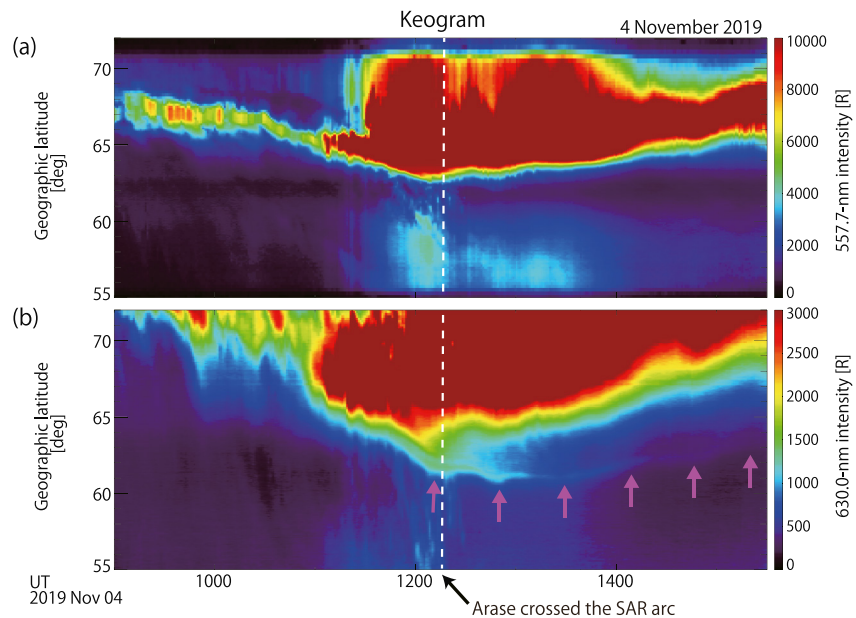


Figure 11. Keograms obtained by slicing (a) 557.7-nm and (b) 630.0-nm auroral images at Gakona in meridional direction at longitude of Gakona from ~0900 to ~1530 UT on November 4, 2019. The pink arrows in (b) indicate the location of the SAR arc. The vertical white dashed line shows when the Arase satellite crossed the SAR arc. SAR, stable auroral red.

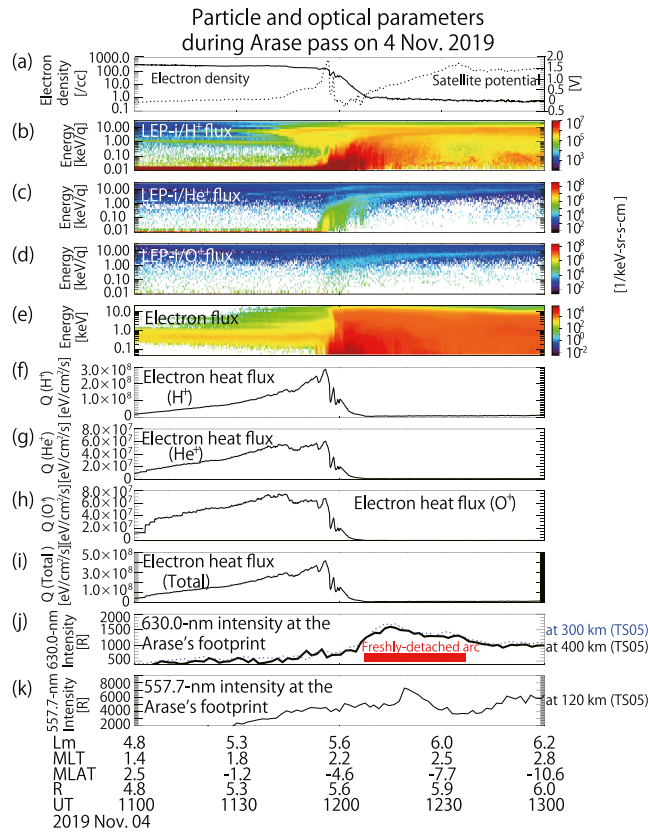


Figure 12. From top to bottom: (a) electron density calculated from UHR frequency (solid curve) and satellite potential (dashed curve); (b) omnidirectional H^+ flux (LEP-i); (c) omnidirectional He^+ flux (LEP-i); (d) omnidirectional O^+ flux (LEP-i); (e) omnidirectional electron flux (LEP-e); electron heat flux estimated from Coulomb collisions between electrons and (f) H^+ , (g) He^+ , and (h) O^+ ; (i) total heat flux; (j) 630.0-nm and (k) 557.7-nm airglow/auroral intensities observed at Gakona in Arase footprint. LEP-e, Low-Energy Particle Experiments-Ion Mass Analyzer; UPR, upper hybrid resonance.

Figures 13h–13j show the dynamic spectra of the magnetic-field observed by Arase/MGF (64-Hz data) in the frequency range of 0.1–30 Hz. The three magnetic-field components in SM coordinates are shown in Figures 13h–13j, respectively. The local cyclotron frequencies of H^+ , He^+ , and O^+ are plotted in these panels as a reference to examine EMIC-wave activity. Figures 13h–13j show several horizontal band enhancements of PSDs at fixed frequencies of ~ 0.3 – 0.7 Hz (between the cyclotron frequencies of He^+ and O^+) at ~ 1100 – 1150 UT. These band enhancements are considered to be artificial noise because their frequencies are constant. In Figure 13h and 13i, broadband PSD enhancements were observed at 1130–1140 UT, and these also seem to be noise. In Figure 13h and 13j, weak increases in PSD were observed at ~ 1 Hz at ~ 1145 UT and at 0.2–0.6 Hz at ~ 1200 UT. These enhancements may have been due to real electromagnetic waves. The increase of PSD at ~ 1200 UT seems to correspond to the local increase of electron flux; the PSDs then were rather weak, with an amplitude of $\sim 10^{-2}$ nT²/Hz.

Figures 13k and 13m show the electron flux with a pitch angle of $\sim 174.4^\circ$ observed by MEP-e and LEP-e, respectively. Because the satellite was located 4.6° south of the magnetic equator as shown below the horizontal axis (MLAT), the flux with a pitch angle of 174.4° is evaluated assuming that the aurora observed on the ground also appeared at the conjugate point in the Southern Hemisphere. There were local electron-flux enhancements at energies of <200 eV and 10–20 keV with pitch angles near the loss cone. The black dashed and solid curves in Figure 13m show the electron density estimated from the UHR frequency and the ECH intensity observed in Figure 13b. The ECH intensity was derived by integrating the PSDs in frequencies of 1 – $2f_{ce}$ (e.g., Fukizawa et al., 2018). The contaminated and calibration parts were linearly interpolated. These curves suggest that the increase of electron flux <200 eV was observed in the spatial overlap between the electron density gradient and the ECH generation region.

6.3. DMSP Observations

The ionospheric responses associated with the SAR arc are shown in Figures 14 and 15. Figure 14 shows the data observed as DMSP-F15 crossed the SAR arc at ~ 1325 UT. Figure 14a includes a 630-nm image taken at 1324:50 UT and a plot of the footprint of the 400-km altitude mapping of the DMSP-F15 position using the IGRF-12 model. The emission intensity at the pixels of the footprint is shown in Figure 14e to identify the position of the SAR arc as a clear peak. The red vertical dashed line in Figures 14b–14e represents the SAR-arc peak. The satellite altitude, MLT, MLAT, and UT of DMSP-F15 are shown below the horizontal axis. The MLT and MLAT values are those at the original flying altitude.

Figure 14b shows that the SAR-arc peak with an intensity of ~ 1.8 kR was located at the minimum of ionospheric density trough. Figure 14c shows that there was a weak eastward and upward ion flow at the SAR-arc peak. Figure 14d shows a substantial T_e rise up to ~ 9000 K at the SAR arc. In Figure 14b, the electron density increases slightly to the left of the red dashed line (slightly poleward of the T_e enhancement in the ionosphere). The data of precipitating particle flux is not available during the time interval shown in Figures 14b–14e.

Figure 15 shows the observations from DMSP-F16 as it crossed the SAR arc at ~ 1434 UT. Figure 15a shows the footprint mapping of the DMSP-F16 position to 400-km altitude using the IGRF-12 model, and a 630-nm image taken at 1424:50 UT. The emission intensities along the pixels of the footprint are indicated in Figure 15g to clarify the SAR-arc position. The red vertical dashed line in Figures 15b–15g indicates the SAR-arc peak.

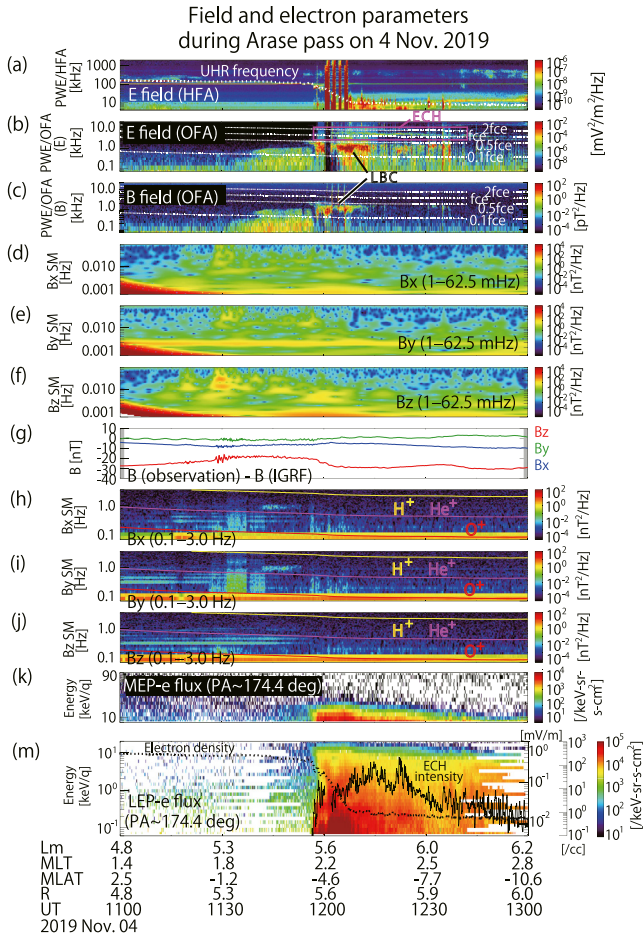


Figure 13. From top to bottom, (a) electric-field spectra obtained by PWE/HFA; (b) electric-field spectra obtained by PWE/OFA; (c) magnetic-field spectra obtained by PWE/OFA; (d)–(f) wavelet spectra of magnetic field at frequencies of 1–62.5 mHz; (g) magnetic perturbations (time resolution: 8 s) obtained by subtracting IGRF-13 model; (h)–(j) fast-Fourier-transform spectra of magnetic field at frequencies of 0.1–3.0 Hz observed by MGF; (k, m) electron flux with pitch angle of $\sim 174.4^\circ$ observed by MEP-e and LEP-e, respectively, all measured by Arase satellite during crossing of freshly detached SAR arc at ~ 1215 UT. The white dotted curve in Figure 13a shows the UHR frequency. The white curves in Figure 13b and 13c indicate the local electron cyclotron frequency (f_{ce}), $0.5f_{ce}$, and $0.1f_{ce}$. The yellow, pink, and red curves in Figures 13h–13j represent the gyro-frequencies of H^+ , He^+ , and O^+ , respectively, at the satellite's position. The black curves in Figure 13m show the electron density estimated from the UHR frequency (dashed) and the ECH intensity observed in Figure 13b (solid). ECH, electron cyclotron harmonic; HFA, High-Frequency Analyzer; IGRF, International Geomagnetic Reference Field; LEP-e, Low-Energy Particle Experiments-Electron Analyzer; MEP-e, Magnetic Field Experiment; Medium-Energy Particle Experiments-Electron Analyzer; OFA, Onboard Frequency Analyzer; PWE, Plasma Wave Experiment; SAR, stable auroral red; UHR, upper hybrid resonance.

Figure 15b and 15c show the electron and ion fluxes, respectively. The SAR-arc peak was located at the equatorward boundary of the electron precipitation region, as shown in Figure 15b. No particular variation of the ion flux is seen at the SAR arc, as evident from Figure 15c. Figure 15d shows that the SAR-arc peak with an intensity of ~ 500 R was located at the ionospheric trough minimum. Figure 15e indicates that there was a very weak eastward and upward ion flow at the SAR-arc peak. Figure 15f shows a high Te increase up to ~ 7000 K at the SAR arc. In Figure 15d, the electron density increases slightly to the left of the red dashed line (slightly poleward of the Te enhancement in the ionosphere), similarly to that in Figure 14b. Although not shown herein, a similar enhancement of electron density was observed at slightly higher latitudes than those for the increases in Te associated with the SAR arc, namely when F15 crossed the SAR arc at ~ 1504 UT and when F18 crossed the SAR arc at ~ 1522 UT. These facts suggest that the electron density increased locally just poleward of the Te enhancements in the present event.

6.4. Discussion

The freshly detached SAR arc that Arase encountered was not a conventional SAR arc because a strong green-line emission (~ 7 kR) accompanied the red arc (2 kR). However, the arc later became a SAR arc with dominant 630-nm emission. The 630-nm arc existed continuously for ~ 2 h 30 m, as shown in Movie S3; this is the average lifetime of substorm-associated SAR arcs (e.g., Takagi et al., 2018). The observations made when DMSP crossed this arc at later times also show clear characteristics of a SAR arc (i.e., localized Te enhancement in the ionospheric trough). Thus, we conclude that this freshly detached 630.0-nm arc became a SAR arc later, and we refer to that arc as a “freshly detached SAR arc.”

As shown in Figure 12b, 12c, and 12e, flux enhancements of H^+ , He^+ , and electrons at energies below 1 keV were observed above the freshly detached SAR arc. These flux enhancements, particularly that of electrons, can cause auroral emission. We reason that the freshly detached SAR arc accompanied by local green-line emission was caused by two electron-flux components with a pitch angle ($\sim 174.4^\circ$) near the loss cone. Specifically, it is considered that the component of electron flux less than 200 eV produced the red arc, and the local component of 10–20 keV strengthened the green-line emission at the equatorward edge of the diffuse aurora, as observed by the ASI (Figure S5).

Figure 13b and 13c show that LBC waves at a frequency of ~ 1 kHz coincided with the electron-flux enhancement. Because LBC waves are known to scatter electrons with energies of kiloelectronvolts to tens of kiloelectronvolts and cause diffuse aurora (e.g., Miyoshi et al., 2015, 2020; Thorne et al., 2010), they may have caused the observed increase of electron flux at energies of 10–20 keV with pitch angles near the loss cone and intensified the 557.7-nm emission at the equator edge of the diffuse aurora.

Figure 13b shows that ECH waves were observed, which can resonate with electrons from a few hundred electronvolts to a few kiloelectron-

volts via cyclotron resonance (e.g., Ashour-Abdalla & Kennel, 1978; Ashour-Abdalla et al., 1979; Horne et al., 2003). Kazama et al. (2018) showed that ECH waves are associated with (i) enhancement of electron flux at energies of ~ 91 eV and (ii) depletion of electron density. The ECH intensity shown in Figure 13m may have contributed to the increase of electron flux (<1 keV). Where the electron density is relatively high (density gradient region) and the ECH waves overlap, an increase in electron flux (<200 eV) was observed;

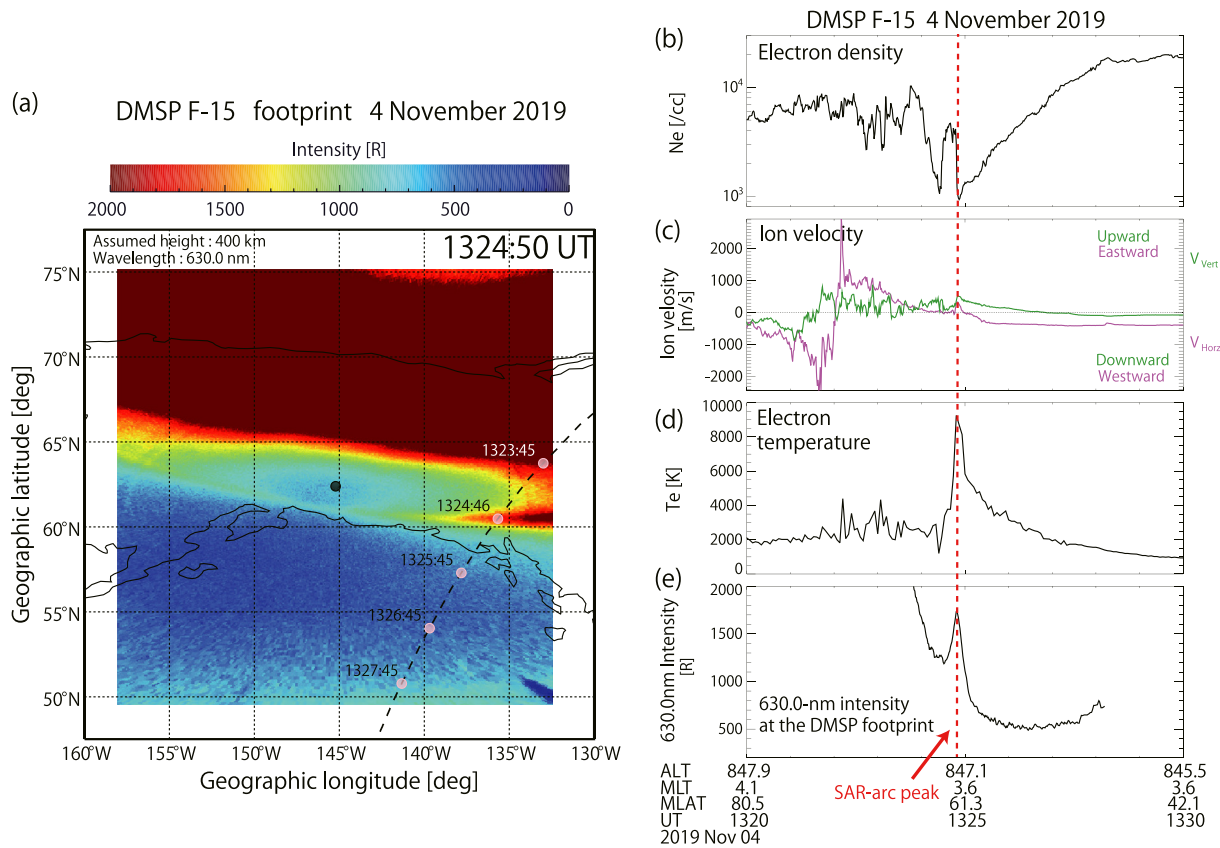


Figure 14. (a) 630-nm image captured with airglow ASI at Gakona on November 4, 2019 at 1324:50 UT; (b) electron density, (c) vertical (green) and horizontal (pink) ion velocity, and (d) electron temperature, all observed by DMSP-F15 satellite; (e) 630.0-nm airglow/auroral intensity observed at Athabasca near the DMSP-F15 footprint. The image in (a) was converted to geographical coordinates by assuming 630-nm emission altitude of 400 km. The black dashed curve shows the trajectory of the footprint of the DMSP-F15 satellite mapped at an altitude of 400 km using the IGRF-12 model. The pink dots in (a) indicate the positions of the footprint of DMSP-F15 at the times shown left of them. The black dot at the center of the image in (a) indicates the location of the Gakona station. ASI, all-sky imager; DMSP, Defense Meteorological Satellite Program; IGRF, International Geomagnetic Reference Field.

this suggests that the energy of ring-current electrons is transferred to plasmaspheric electrons through ECH waves and becomes a heat source for the SAR arc. Although the interaction between ring-current ions and the plasmasphere has been considered to be important, the overlap of ring-current electrons and the plasmasphere may also be important. Upper-band chorus (UBC) waves ($0.5-1f_{ce}$) can also resonate with electrons at energies from ~ 100 eV to 2 keV and cause diffuse aurora (Ni et al., 2008; Ni, Thorne, Meredith, et al., 2011; Thorne et al., 2010), but no UBC waves were observed, as shown in Figure 13b and 13c.

Based on Figures 13d–13g, we also examine KAWs (ULF waves). As discussed in Section 6.2, Arase observed PSD enhancements of the magnetic field at frequencies of 7–10 mHz, as shown in Figure 13f. This PSD enhancement is close to the location of the electron-flux enhancement. These observations suggest that KAWs may increase the electron, H^+ , and He^+ fluxes around the inner edge of the plasma sheet. However, it is difficult to consider the 7–10-mHz waves as being the main source of the SAR arc because PSDs with similar intensity were observed also at other times (e.g., 1120–1130 UT) in the plasmasphere, and not exclusively at the SAR arc.

The enhancement of the PSDs of EMIC waves at 0.2–0.6 Hz at ~ 1200 UT may also have been related to the freshly detached SAR arc. However, the amplitude of the PSD enhancement was $\sim 10^{-2}$ nT²/Hz, which may be too weak to heat cold electrons (Yuan et al., 2014). Additionally, the pitch-angle distribution of the observed electrons at energies below 200 eV in Figure 13k does not appear to be scattered (e.g., Figure S6). Thus, we conclude that the Landau damping of EMIC waves did not contribute to the generation of the local enhancement of electron flux observed at ~ 1200 UT. Instead, these PSD enhancements at the EMIC frequency ranges may have been caused by the local enhancements of H^+ and He^+ fluxes observed at ~ 1200

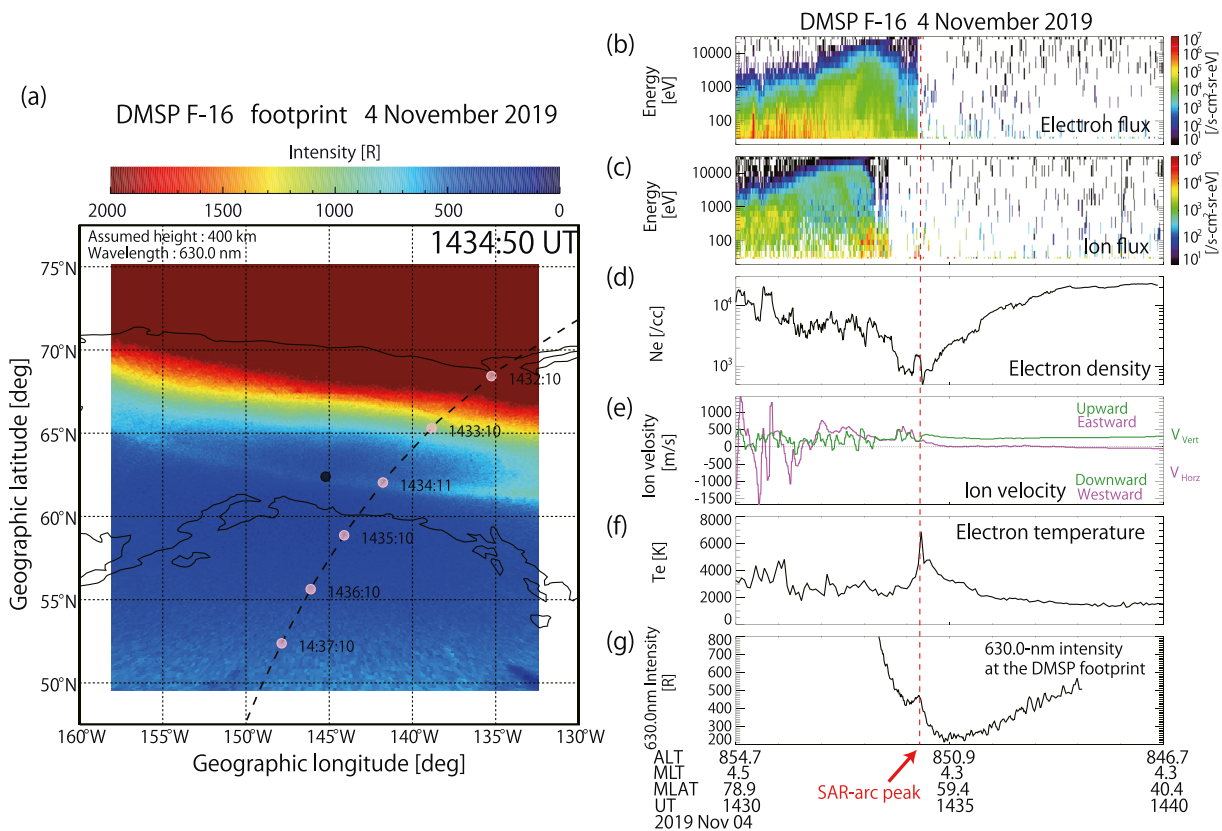


Figure 15. (a) 630-nm image captured with airglow ASI imager at Gakona on November 4, 2019 at 1434:50 UT; energy-time spectrograms of (b) precipitating electron flux and (c) ion flux, (d) electron density, (e) vertical (green) and horizontal (pink) ion velocity, and (f) electron temperature, all observed by DMSP-F16 satellite; (g) 630.0-nm airglow/auroral intensity observed at Athabasca in DMSP-F16 footprint. The pink dots in (a) indicate the positions of the footprint of DMSP-F16 at the time shown to their right. ASI, all-sky imager; DMSP, Defense Meteorological Satellite Program.

UT, as shown in Figure 12b and 12c, because EMIC waves are generated by the energetic ring-current ions with temperature anisotropy near the magnetic equator (e.g., Lu & Wang, 2006; Mauk & McPherron, 1980).

As well as evaluating electromagnetic waves, we discuss the relationship between the satellite potential and the enhancements of e^- and H^+ flux. Satellite potential is related to electron density and T_e (e.g., Davis et al., 2008). Referring to Figure 6 of Inaba et al. (2020), there is a good correspondence between the behaviors of electron density (UHR frequency) and the satellite potential. In Figure 12a of the present study, by contrast, the behaviors of electron density fluctuations estimated from the UHR frequency and the satellite potential change greatly differ at 1155–1230 UT. If the electron density calculated from the upper frequency limit of UHR waves is correct, then large difference between the behaviors of electron density and the satellite potential may indicate ambient T_e variations at the same time. This difference is particularly noticeable at 1157–1207 UT, when the flux enhancements at energies below 200 eV were observed. This T_e increase is likely to correspond to the increase of the strong flux (<200 eV), which is inferred to be associated with ECH or ULF waves, rather than with heat flux due to Coulomb collisions. This fact suggests that ECH (ULF) waves could be a heat source.

The DMSP observations in Figures 14 and 15 show that the electron density increased slightly poleward of the T_e enhancements, and the SAR arc formed in the shared region between the density plume and the T_e enhancements. This fact suggests that the electron-density enhancement in this shared region is a common phenomenon that is related to the generation of SAR arcs. Inaba et al. (2020) found on the basis of measurements by the Swarm satellite that the electron density increased at the location of a SAR arc with T_e enhancement. These observations suggest the enhancement of plasma density near a SAR arc and a plasma supply from the magnetosphere.

We reason that the small discrepancy between the positions of the freshly detached SAR arc and the local enhancement of electron flux is due to ambiguity of the field-line mapping from the Arase altitude to the ionosphere. Figure 1f shows that the freshly detached SAR arc was observed at the growth and recovery phase of substorms, and Figure 13g shows that B_z decreased locally at ~ 1200 UT. These geomagnetic observations strongly suggest that the magnetic field varied dynamically in association with substorms, and the TS05 model may not reproduce the geomagnetic-field configuration accurately. Figure 13k and 13m indicate that Arase observed electron-flux enhancements at energies less than 200 eV and 10–20 keV with pitch angles near the loss cone at ~ 1157 – 1207 UT. We reason that these local enhancements correspond to the observed freshly detached red arc and the intensified 557.7-nm emission at the equatorward edge of the diffuse aurora, as observed by the ground-based camera.

7. Summary and Discussion

This study reports on three events in which RBSP and Arase satellites crossed SAR arcs near the equatorial plane of the inner magnetosphere at $L = 5.1$ – 6.0 . The observed characteristics of the three SAR-arc events analyzed in this study are summarized as follows.

Event 1: The RBSP-B satellite crossed a weak SAR arc. Only at the crossing, the heat flux to the ionosphere increased to a value comparable to that of Kozyra et al. (1993, 1997). However, there was no PSD enhancement in the magnetic-field data in the millihertz and hertz wave bands associated with the SAR arc, indicating that EMIC waves and KAWs were not the source of the observed SAR arc. From these facts, this SAR arc was very likely to have been caused by the heat flux generated by the Coulomb collisions between ring-current ions and plasmaspheric electrons.

Event 2: The RBSP-A satellite skimmed along the plasmopause for more than 4 h. At ~ 0600 and ~ 1015 UT, the estimated heat fluxes to the ionosphere increased to a value comparable to that of Kozyra et al. (1993, 1997). However, the SAR arc occurred only at ~ 1015 UT, and we reason that this was due to differences in the ionospheric plasma density, that is, at 1015 UT, the heat flux flowed into the ionospheric trough where effective heating of electrons occurred because there was less ionospheric cooling. Frequency analysis of electromagnetic waves in the 0.1–3.0-Hz range showed that EMIC waves were unlikely to have caused the observed SAR arc. In the millihertz range, 7–20-mHz electromagnetic waves were observed; although their amplitude was as small as 0.9 nT (peak to peak), this is the first time that an inner magnetospheric satellite has observed electromagnetic waves around 10 mHz, only above a SAR arc, while ~ 10 -mHz hydromagnetic waves were observed simultaneously with SAR arcs by ground observation (Lanzerotti et al., 1978). These facts again indicate that Coulomb collisions are the most plausible mechanism for the generation of this SAR arc. The 7–20-mHz electromagnetic waves may have a minor contribution to the heat flux in this case. However, the observed amplitude of 0.9 nT (peak to peak) seems to be too weak to contribute to the electron heating.

Event 3: The Arase satellite passed over an auroral arc that was freshly detached from the auroral oval and consisted of both 557.7- and 630.0-nm emissions. Later, this arc evolved to a SAR arc characterized by only the 630.0-nm emission. Thus, we refer to this arc as a “freshly detached SAR arc.” We conclude that the component of electron flux at energies less than 200 eV produced the freshly detached SAR arc. The localized 10–20-keV electron-flux enhancement intensifies the green-line emission at the equatorward edge of the diffuse aurora. These flux enhancements were accompanied by the flux enhancements of H^+ , and He^+ (<1 keV), ECH, LBC, weak EMIC, and 7–10-mHz ULF waves. We reason that the local green-line emission appeared in the same position as the red arc because various electromagnetic waves occurred with substorm. In addition, although the DMSP data indicated a T_e increase up to ~ 9000 K, the heat flux estimated from magnetospheric observations was not sufficient to cause the SAR arc. It may be possible that the ECH waves, which have not been previously implicated, caused scattering of low-energy (<1 keV) electrons, resulting in the ionospheric heating (e.g., Kazama et al., 2018; Thorne et al., 2010). The mechanisms that cause of the observed increase of proton and helium ion flux needs further study.

Table 1 summarizes the maximum heat fluxes for the three events estimated from ion fluxes and plasmaspheric densities measured by the RBSP and Arase satellites. The heat fluxes of events 1 and 2 are comparable but slightly smaller than those of past studies ($\sim 8.0 \times 10^9$ – 1.0×10^{10} eV/cm²/s in winter during

Table 1
Maximum Heat Fluxes Estimated for Three SAR-Arc Events Using RBSP and Arase

Event #	Date	Time	Heat flux	630.0-nm intensity
Event 1	December 19, 2012	~1055 UT	$\sim 2.5 \times 10^9$ eV/cm ² /s	~65 R
Event 2	January, 17 2015	~1015 UT	$\sim 5.0 \times 10^9$ eV/cm ² /s	~110 R
Event 3	November 4, 2019	~1215 UT	$\sim 4.0 \times 10^8$ eV/cm ² /s	~1.5 kR

solar maximum, as estimated by Kozyra et al. (1987, 1990)). Kozyra et al. (1987) estimated the heat fluxes by using a plasmaspheric model and ion-flux data observed by the DE-1 satellite, and Kozyra et al. (1990) calculated the required heat fluxes using an ionospheric and atmospheric model. The discrepancy between the present study and the past studies suggests that the heat fluxes estimated based on direct observations are slightly smaller than those predicted using the models.

We also discuss the possible cause of the slight shortage of heat flux and the occurrence of SAR arcs during non-storm-time substorms for the three events.

The somewhat smaller heat flux than expected may have been supplemented by the 7–20-mHz ULF waves with an amplitude (peak to peak) of 0.9 nT observed in event 2 and the enhancement of the electron flux at energies below 200 eV observed in event 3. Further quantitative studies, including the role of ECH waves for SAR-arc generation, are needed to test this hypothesis. We also note that the most intense and latitudinally widest emissions in event 3 were on the eastern edge of the SAR arc, which is opposite to what we would expect from the expected “bulge” shape of the plasmasphere (e.g., Ievenko, 2020). When Arase crossed the thick part of the SAR arc of event 3 at the eastern edge, it was located at ~2.2 MLT, which is opposite to the dusk-premidnight region where SAR arcs are often observed (Takagi et al., 2018). According to Ni, Thorne, Liang, et al. (2011), ECH waves are limited to the magnetic equatorial plane and often occur at 21–6 MLT. Assuming that the SAR arc of event 3 is associated with ECH, the ECH waves observed at postmidnight may have intensified and latitudinally broadened the eastern part of the SAR arc.

Similar to event 3, the SAR arcs in events 1 and 2 were observed at ~3 and 2.4 MLT, respectively, during non-storm-time substorms. A statistical study of dispersionless substorm injections by Perry et al. (1996) found that non-storm-time substorms ($Dst > -30$ nT) tend to occur more on the eastern side compared with storm-time substorms ($Dst \leq -30$ nT). This suggests that the eastward shift of injection location during non-storm-time substorms may be related to the postmidnight SAR arc in the present study. Interestingly, He et al. (2017) showed that subauroral polarization streams (SAPSs) during quiet-time substorms are likely to occur more on eastern side than SAPSs during storm-time substorms, suggesting a possible relationship with non-storm-time SAR arcs.

The observed SAR arc events in this study are different from typical SAR arcs because they were observed during non-storm times. This may have been the reason for the smaller heat fluxes. According to the relationship between heat flux and SAR-arc emission intensity in winter during solar maximum discussed by Kozyra et al. (1997), the heat flux is estimated to be larger than the SAR-arc emission intensity when a large storm occurs. Kozyra et al. (1990, 1997) also showed the relationship between SAR-arc intensity and heat flux in fall during solar minimum, which is very similar to that found in the present study. This fact may suggest that the SAR arcs in the present events occurred under conditions close to those of the ionosphere and atmosphere in fall during solar minimum.

Our results indicate that although Coulomb collisions are the most plausible mechanism for generating SAR arcs, the latter cannot be explained by the former alone, and electromagnetic or electrostatic waves are sometimes observed with SAR arcs. The occurrence of SAR arcs during non-storm-time substorms has been a topic attracting less attention than those during storm time. Our observations require further understanding not only of SAR-arc generation but also of the magnetosphere-thermosphere-ionosphere coupling process during non-storm-time and storm-time substorms.

Data Availability Statement

The SYM-H, AU, and AL indices were provided by the World Data Center (WDC) for Geomagnetism at Kyoto University, Japan. The PWING observation data and geomagnetic indices (AE and SYM-H) are distributed by the Inter-university Upper atmosphere Global Observation Network (IUGONET) project of the Ministry of Education, Culture, Sports, Science and Technology of Japan. The ground-based THEMIS magnetometer data can be obtained through <http://themis.ssl.berkeley.edu/data/themis/thg/12/mag/>. The RBSP/HOPE and RBSP/EMFISIS data used in this study were downloaded from the RBSP ECT and EMFISIS websites at http://www.rbsp-ect.lanl.gov/rbsp_ect.php and <https://emfisis.physics.uiowa.edu/data/index>. The scientific data of the ERG (Arase) satellite were obtained from the ERG Science Center (ERG-SC) operated by ISAS/JAXA and ISEE/Nagoya University (<https://ergsc.isee.nagoya-u.ac.jp/index.shtml.en>; Miyoshi, Hori, et al., 2018). The present study analyzed LEP-e-L2 omniflux v02_02 data (S.-Y. Wang et al., 2018), LEP-e-L3 PAD v02_01 data, LEP-i-L2 omniflux v02_02 data (Asamura et al., 2018a), LEP-i-L2 3dflux v03_00 (Asamura et al., 2018b), MEP-e-L2 omniflux v01_02 data (Kasahara et al., 2018b), MEP-e-L2 3dflux v01_01 data (Kasahara et al., 2018a), MEP-i-L2 3dflux v02_00 data (Yokota et al., 2018), PWE/EFD/pot-L2 v03_01 data (Kasahara, Kasaba, Matsuda, et al., 2018), PWE/HFA-L2 v01_02 (Kasahara, Kumamoto, et al., 2018), PWE/OFA-L2 v02_01 (Kasahara, Kojima, et al., 2018) and MGF-L2 8sec v04_04 data (Matsuoka et al., 2018a), MGF/64-Hz-L2 v04_04 data (Matsuoka et al., 2018b), and L2 v03 orbit data (Miyoshi, Shinohara, & Jun, 2018). The optical data from Athabasca and Gakona stations are available from the ISEE through the ERG-SC. The DMSP observation data were provided by the Madrigal CEDAR Database and Boston College, Institute for Scientific Research (<http://cedar.openmadrigal.org>). The OMNI data were provided by the GSFC/SPDF OMNIWeb interface (<http://omniweb.gsfc.nasa.gov>). The solar wind parameters and W-parameters for driving the TS05 model were provided by the TS05 web repository (http://geo.phys.spbu.ru/~tsyganenko/TS05_data_and_stuff/). The GNSS-TEC data providers are listed at http://stdb2.isee.nagoya-u.ac.jp/GPS/GPS-TEC/gnss_provider_list.html; the main ones were UNAVCO (<https://www.unavco.org/data/gps-gnss/gps-gnss.html>), CDDIS (<https://cddis.nasa.gov/archive/gnss/data/daily/>; Noll, 2010), CHAIN (http://chain.physics.unb.ca/chain/pages/data_download; Jayachandran et al., 2009), PANGA (<http://www.geodesy.cwu.edu>; Pacific Northwest Geodetic Array (PANGA), 1996), SOPAC (<ftp://garner.ucsd.edu/pub/rinex/>), SONEL (<https://www.sonel.org/-GPS-.html>), and NCEDC (<https://ncedc.org/bard.overview.html>; NCEDC, 2014).

Acknowledgments

The authors thank Y. Kato, H. Hamaguchi, Y. Yamamoto, and T. Adachi of ISEE, Nagoya University for their continuous support of the all-sky imager operation. The authors also thank the RBSP/EMFISIS team for providing the data. The operation of the airglow imager at Gakona was supported by the University of Alaska, Fairbanks. Athabasca University GeoSpace Observatory was constructed and is operated with support from the Canada Foundation for Innovation. This work was supported by Grants-in-Aid for Scientific Research (15H05815, 15H05747, 16H06286, 20H01959, and 20H01955) from the Japan Society for the Promotion of Science. Part of the work of Y. Miyoshi, T. Hori, and M. Shoji was performed at ERG-SC. Most of the data analysis for satellites and imagers was conducted using the Space Physics Environment Data Analysis Software (SPEDAS) tool (Angelopoulos et al., 2019).

References

- Anderson, B. J., Erlandson, R. E., & Zanetti, L. J. (1992). A statistical study of Pc 1–2 magnetic pulsations in the equatorial magnetosphere: 1. Equatorial occurrence distributions. *Journal of Geophysical Research*, 97, 3075–3088. <https://doi.org/10.1029/91ja02706>
- Anderson, B. J., Erlandson, R. E., & Zanetti, L. J. (1992). A statistical study of Pc 1–2 magnetic pulsations in the equatorial magnetosphere: 2. Wave properties. *Journal of Geophysical Research*, 97, 3089–3101. <https://doi.org/10.1029/91ja02697>
- Angelopoulos, V., Cruce, P., Drozdov, A., Grimes, E. W., Hatzigeorgiu, N., King, D. A., et al. (2019). The Space Physics Environment Data Analysis System (SPEDAS). *Space Science Reviews*, 215, 9. <https://doi.org/10.1007/s11214-018-0576-4>
- Asamura, K., Kazama, Y., Yokota, S., Kasahara, S., & Miyoshi, Y. (2018). Low-energy particle experiments-ion mass analyzer (LEPi) on-board the ERG (Arase) satellite. *Earth Planets and Space*, 70, 70. <https://doi.org/10.1186/s40623-018-0846-0>
- Asamura, K., Miyoshi, Y., & Shinohara, I. (2018a). The LEPi instrument level-2 3D flux data of Exploration of energization and Radiation in Geospace (ERG) Arase satellite, Version v03.00. ERG Science Center, Institute for Space-Earth Environmental Research, Nagoya University. <https://doi.org/10.34515/DATA.ERG-05000>
- Asamura, K., Miyoshi, Y., & Shinohara, I. (2018b). The LEPi instrument level-2 omniflux data of Exploration of energization and Radiation in Geospace (ERG) Arase satellite, Version v03.00. ERG Science Center, Institute for Space-Earth Environmental Research, Nagoya University. <https://doi.org/10.34515/DATA.ERG-05001>
- Ashour-Abdalla, M., & Kennel, C. F. (1978). Nonconvective and convective electron cyclotron harmonic instabilities. *Journal of Geophysical Research*, 83(A4), 1531–1543. <https://doi.org/10.1029/JA083iA04p01531>
- Ashour-Abdalla, M., Kennel, C. F., & Livesey, W. (1979). A parametric study of electron multiharmonic instabilities in the magnetosphere. *Journal of Geophysical Research*, 84, 6540–6546. <https://doi.org/10.1029/JA084iA11p06540>
- Barbier, D. (1958). The auroral activity at low latitudes. *Annals of Geophysics*, 1, 4334–4355. <https://doi.org/10.1051/apido:19580201>
- Chu, X., Malaspina, D., Gallardo-Lacourt, B., Liang, J., Andersson, L., Ma, Q., et al. (2019). Identifying STEVE's magnetospheric driver using conjugate observations in the magnetosphere and on the ground. *Geophysical Research Letters*, 46, 12665–12674. <https://doi.org/10.1029/2019gl082789>
- Cole, K. D. (1965). Stable auroral red arcs, sinks for energy of Dst main phase. *Journal of Geophysical Research*, 70, 1689–1706. <https://doi.org/10.1029/JZ070i007p01689>
- Cornwall, J. M., Coroniti, F. V., & Thorne, R. M. (1971). Unified theory of SAR arc formation at the plasmapause. *Journal of Geophysical Research*, 76, 4428–4445. <https://doi.org/10.1029/ja076i019p04428>
- Davis, V. A., Mandell, M. J., & Thomsen, M. F. (2008). Representation of the measured geosynchronous plasma environment in spacecraft charging calculations. *Journal of Geophysical Research*, 113, A10204. <https://doi.org/10.1029/2008JA013116>

- Foster, J. C., Buonsanto, M. J., Mendillo, M., Nottingham, D., Rich, F. J., & Denig, W. (1994). Coordinated stable auroral red arc observations: Relationship to plasma convection. *Journal of Geophysical Research*, 99, 11429–11439. <https://doi.org/10.1029/93ja03140>
- Fukizawa, M., Sakanai, T., Miyoshi, Y., Hosokawa, K., Shiokawa, K., Katoh, Y., et al. (2018). Electrostatic electron cyclotron harmonic waves as a candidate to cause pulsating auroras. *Geophysical Research Letters*, 45, 12661–12668. <https://doi.org/10.1029/2018gl080145>
- Funsten, H. O., Skoug, R. M., Guthrie, A. A., MacDonald, E. A., Baldonado, J. R., Harper, R. W., et al. (2013). Helium, Oxygen, Proton, and Electron (HOPE) mass spectrometer for the radiation belt storm probes mission. *Space Science Reviews*, 179, 423–484. <https://doi.org/10.1007/s11214-013-9968-7>
- Greenspan, M. E., Anderson, P. B., & Pelagatti, J. M. (1986). *Characteristics of the thermal plasma monitors (SSIES) for the Defense Meteorological Satellite Program (DMSP) spacecraft S8 through F10* Technical Report AFGL-TR-86-0227. Bedford, MA: Air Force Geophysics Laboratory, Hanscom Air Force Base.
- Hasegawa, A., & Mima, K. (1978). Anomalous transport produced by kinetic Alfvén wave turbulence. *Journal of Geophysical Research*, 83, 1117–1123. <https://doi.org/10.1029/ja083ia03p01117>
- He, F., Zhang, X.-X., Wang, W., & Wan, W. (2017). Different evolution patterns of subauroral polarization streams (SAPS) during intense storms and quiet time substorms. *Geophysical Research Letters*, 44, 10796–10804. <https://doi.org/10.1002/2017GL075449>
- Horne, R. B., Thorne, R. M., Meredith, N. P., & Anderson, R. R. (2003). Diffuse auroral electron scattering by electron cyclotron harmonic and whistler mode waves during an isolated substorm. *Journal of Geophysical Research*, 108(A7), 1290. <https://doi.org/10.1029/2002ja009736>
- Ievenko, I. B. (2020). SAR arc observation during the overlap registration of an energetic plasma with a plasmopause aboard the Van Allen Probe. *Journal of Atmospheric and Solar-Terrestrial Physics*, 209, 105386. <https://doi.org/10.1016/j.jastp.2020.105386>
- Inaba, Y., Shiokawa, K., Oyama, S., Otsuka, Y., Oksanen, A., Shinbori, A., et al. (2020). Plasma and field observations in the magnetospheric source region of a stable auroral red (SAR) arc by the Arase satellite on March 28, 2017. *Journal of Geophysical Research: Space Physics*, 125. <https://doi.org/10.1029/2020ja028068>
- Iyemori, T. (1990). Storm-time magnetospheric currents inferred from midlatitude geomagnetic field variations. *Journal of Geomagnetism and Geoelectricity*, 42, 1249–1265. <https://doi.org/10.5636/jgg.42.1249>
- Iyemori, T., & Rao, D. R. K. (1996). Decay of the Dst field of geomagnetic disturbance after substorm onset and its implication to storm-substorm relation. *Annals of Geophysics*, 14, 608–618. <https://doi.org/10.1007/s00585-996-0608-3>
- Jayachandran, P. T., Langley, R. B., MacDougall, J. W., Mushini, S. C., Pokhotelov, D., Hamza, A. M., et al. (2009). Canadian High Arctic Ionospheric Network (CHAIN). *Radio Science*, 44, RS0A03. <https://doi.org/10.1029/2008RS004046>
- Jordanova, V. K., Kistler, L. M., Kozyra, J. U., Khazanov, G. V., & Nagy, A. F. (1996). Collisional losses of ring current ions. *Journal of Geophysical Research*, 101, 111–126. <https://doi.org/10.1029/95ja02000>
- Kasaba, Y., Ishisaka, K., Kasahara, Y., Imachi, T., Yagitani, S., Kojima, H., et al. (2017). Wire probe antenna (WPT) and electric field detector (EFD) of plasma wave experiment (PWE) aboard the Arase satellite: Specifications and initial evaluation results. *Earth Planets and Space*, 69, 174. <https://doi.org/10.1186/s40623-017-0760-x>
- Kasahara, S., Yokota, S., Hori, T., Keika, K., Miyoshi, Y., & Shinohara, I. (2018a). *The MEP-e instrument level-2 3-D flux data of Exploration of energization and Radiation in Geospace (ERG) Arase satellite, Version v01.01*. ERG Science Center, Institute for Space-Earth Environmental Research, Nagoya University. <https://doi.org/10.34515/DATA.ERG-02000>
- Kasahara, S., Yokota, S., Hori, T., Keika, K., Miyoshi, Y., & Shinohara, I. (2018b). *The MEP-e instrument level-2 omni-directional flux data of Exploration of energization and Radiation in Geospace (ERG) Arase satellite, Version v01.01*. ERG Science Center, Institute for Space-Earth Environmental Research, Nagoya University. <https://doi.org/10.34515/DATA.ERG-02001>
- Kasahara, S., Yokota, S., Mitani, T., Asamura, K., Hirahara, M., Shibano, Y., & Takashima, T. (2018). Medium-energy particle experiments-electron analyzer (MEP-e) for the exploration of energization and radiation in geospace (ERG) mission. *Earth Planets and Space*, 70, 69. <https://doi.org/10.1186/s40623-018-0847-z>
- Kasahara, Y., Kasaba, Y., Kojima, H., Yagitani, S., Ishisaka, K., Kumamoto, A., et al. (2018). The Plasma Wave Experiment (PWE) onboard the Arase (ERG) satellite. *Earth Planets and Space*, 70(1). <https://doi.org/10.1186/s40623-018-0842-4>
- Kasahara, Y., Kasaba, Y., Matsuda, S., Shoji, M., Nakagawa, T., Ishisaka, K., et al. (2018). *The PWE/EFD instrument level-2 spin-averaged potential data of Exploration of energization and Radiation in Geospace (ERG) Arase satellite, Version v04.01*. ERG Science Center, Institute for Space-Earth Environmental Research, Nagoya University
- Kasahara, Y., Kojima, H., Matsuda, S., Ozaki, M., Yagitani, S., Shoji, M., et al. (2018). *The PWE/OFA instrument level-2 spectrum data of Exploration of energization and Radiation in Geospace (ERG) Arase satellite, Version v02.01*. ERG Science Center, Institute for Space-Earth Environmental Research, Nagoya University. <https://doi.org/10.34515/DATA.ERG-08000>
- Kasahara, Y., Kumamoto, A., Tsuchiya, F., Matsuda, S., Shoji, M., Nakamura, S., et al. (2018). *The PWE/HFA instrument level-2 spectrum data of Exploration of energization and Radiation in Geospace (ERG) Arase satellite, Version v01.02*. ERG Science Center, Institute for Space-Earth Environmental Research, Nagoya University. <https://doi.org/10.34515/DATA.ERG-10000>
- Kazama, Y., Kojima, H., Miyoshi, Y., Kasahara, Y., Usui, H., Wang, B.-J., et al. (2018). Density depletions associated with enhancements of electron cyclotron harmonic emissions: An ERG observation. *Geophysical Research Letters*, 45, 10075–10083. <https://doi.org/10.1029/2018gl080117>
- Kazama, Y., Wang, B. J., Wang, S. Y., Ho, P. T. P., Tam, S. W. Y., Chang, T. F., et al. (2017). Low-energy particle experiments-electron analyzer (LEPe) onboard the Arase spacecraft. *Earth Planets and Space*, 69, 165. <https://doi.org/10.1186/s40623-017-0748-6>
- Kessel, R. L., Fox, N. J., & Weiss, M. (2013). The Radiation Belt Storm Probes (RBSP) and space weather. *Space Science Reviews*, 179, 531–543. <https://doi.org/10.1007/s11214-012-9953-6>
- Kletzing, C. A., Kurth, W. S., Acuna, M., MacDowall, R. J., Torbert, R. B., Averkamp, T., et al. (2013). The electric and magnetic field instrument suite and integrated science (EMFISIS) on RBSP. *Space Science Reviews*, 179, 127–181. <https://doi.org/10.1007/s11214-013-9993-6>
- Kozyra, J. U., Chandler, M. O., Hamilton, D. C., Peterson, W. K., Klumpar, D. M., Slater, D. W., et al. (1993). The role of ring current nose events in producing stable auroral red arc intensifications during the main phase: Observations during the September 19–24, 1984, Equinox Transition Study. *Journal of Geophysical Research*, 98, 9267–9283. <https://doi.org/10.1029/92ja02554>
- Kozyra, J. U., Nagy, A. F., & Slater, D. W. (1997). High-altitude energy source(s) for stable auroral red arcs. *Reviews of Geophysics*, 35, 155–190. <https://doi.org/10.1029/96rg03194>
- Kozyra, J. U., Shelley, E. G., Comfort, R. H., Brace, L. H., Cravens, T. E., & Nagy, A. F. (1987). The role of ring current O⁺ in the formation of stable auroral red arcs. *Journal of Geophysical Research*, 92, 7487–7502. <https://doi.org/10.1029/ja092ia07p07487>
- Kozyra, J. U., Valladares, C. E., Carlson, H. C., Buonsanto, M. J., & Slater, D. W. (1990). A theoretical study of the seasonal and solar cycle variations of stable auroral red arcs. *Journal of Geophysical Research*, 95, 12219–12234. <https://doi.org/10.1029/JA095iA08p12219>
- Kumamoto, A., Tsuchiya, F., Kasahara, Y., Kasaba, Y., Kojima, H., Yagitani, S., et al. (2018). High Frequency Analyzer (HFA) of Plasma Wave Experiment (PWE) onboard the Arase spacecraft. *Earth Planets and Space*, 70, 82. <https://doi.org/10.1186/s40623-018-0854-0>

- Lanzerotti, L. J., Hasegawa, A., & MacLennan, C. G. (1978). Hydromagnetic waves as a cause of a SAR arc event. *Planetary and Space Science*, 26, 777–783. [https://doi.org/10.1016/0032-0633\(78\)90008-9](https://doi.org/10.1016/0032-0633(78)90008-9)
- Liou, K., Meng, C.-I., Newell, P. T., Takahashi, K., Ohtani, S.-I., Lui, A. T. Y., et al. (2000). Evaluation of low-latitude Pi2 pulsations as indicators of substorm onset using Polar ultraviolet imagery. *Journal of Geophysical Research*, 105, 2495–2505. <https://doi.org/10.1029/1999JA900416>
- Lu, Q. M., & Wang, S. (2006). Electromagnetic waves downstream of quasi-perpendicular shocks. *Journal of Geophysical Research*, 111, A05204. <https://doi.org/10.1029/2005JA011319>
- MacDonald, E. A., Donovan, E., Nishimura, Y., Case, N. A., Gillies, D. M., Gallardo-Lacourt, B., et al. (2018). New science in plain sight: Citizen scientists lead to the discovery of optical structure in the upper atmosphere. *Science Advances*, 4(3). <https://doi.org/10.1126/sciadv.aag0030>
- Martinis, C., Baumgardner, J., Mendillo, M., Taylor, M. J., Moffat-Griffin, T., Wroten, J., et al. (2019). First ground-based conjugate observations of stable auroral red (SAR) arcs. *Journal of Geophysical Research: Space Physics*, 124, 4658–4671. <https://doi.org/10.1029/2018ja026017>
- Matsuda, S., Kasahara, Y., Kojima, H., Kasaba, Y., Yagitani, S., Ozaki, M., et al. (2018). Onboard software of plasma wave experiment aboard arase: Instrument management and signal processing of waveform capture/onboard frequency analyzer. *Earth Planets and Space*, 70, 75. <https://doi.org/10.1186/s40623-018-0838-0>
- Matsuoka, A., Teramoto, M., Imajo, S., Kurita, S., Miyoshi, Y., & Shinohara, I. (2018a). The MGF instrument level-2 spin-fit magnetic field data of Exploration of energization and Radiation in Geospace (ERG) Arase satellite, Version v03.04. ERG Science Center, Institute for Space-Earth Environmental Research, Nagoya University. Updated daily <https://doi.org/10.34515/DATA.ERG-06001>
- Matsuoka, A., Teramoto, M., Imajo, S., Kurita, S., Miyoshi, Y., & Shinohara, I. (2018b). The MGF instrument level-2 high-resolution magnetic field data of Exploration of energization and Radiation in Geospace (ERG) Arase satellite, Version v03.04. ERG Science Center, Institute for Space-Earth Environmental Research, Nagoya University. <https://doi.org/10.34515/DATA.ERG-06000>
- Matsuoka, A., Teramoto, M., Nomura, R., Nose, M., Fujimoto, A., Tanaka, Y., et al. (2018). The ARASE (ERG) magnetic field investigation. *Earth Planets and Space*, 70(1). <https://doi.org/10.1186/s40623-018-0800-1>
- Mauk, B. H., Fox, N. J., Kanekal, S. G., Kessel, R. L., Sibeck, D. G., & Ukhorskiy, A. (2013). Science objectives and rationale for the Radiation Belt Storm Probes mission. *Space Science Reviews*, 179, 3–27. <https://doi.org/10.1007/s11214-012-9908-y>
- Mauk, B. H., & McPherron, R. L. (1980). An experimental test of the electromagnetic ion cyclotron instability within the earth's magnetosphere. *Physics of Fluids*, 23, 2111. <https://doi.org/10.1063/1.862873>
- McIlwain, C. E. (1961). Coordinates for mapping the distribution of magnetically trapped particles. *Journal of Geophysical Research*, 66, 3681–3691. <https://doi.org/10.1029/jz066i011p03681>
- Mendillo, M., Finan, R., Baumgardner, J., Wroten, J., Martinis, C., & Casillas, M. (2016). A stable auroral red (SAR) arc with multiple emission features. *Journal of Geophysical Research: Space Physics*, 121, 10564–10577. <https://doi.org/10.1002/2016JA023258>
- Mendillo, M., & Wroten, J. (2019). Modeling stable auroral red (SAR) arcs at geomagnetic conjugate points: Implications for hemispheric asymmetries in heat fluxes. *Journal of Geophysical Research: Space Physics*, 124, 6330–6342. <https://doi.org/10.1029/2019ja026904>
- Miyoshi, Y., Hori, T., Shoji, M., Teramoto, M., Chang, T. F., Segawa, T., et al. (2018). The ERG Science Center. *Earth Planets and Space*, 70. <https://doi.org/10.1186/s40623-018-0867-8>
- Miyoshi, Y., Saito, S., Kurita, S., Asamura, K., Hosokawa, K., Sakano, T., et al. (2020). Relativistic electron microbursts as high-energy tail of pulsating aurora electrons. *Geophysical Research Letters*, 47. <https://doi.org/10.1029/2020GL090360>
- Miyoshi, Y., Saito, S., Seki, K., Nishiyama, T., Kataoka, R., Asamura, K., et al. (2015). Relation between fine structure of energy spectra for pulsating aurora electrons and frequency spectra of whistler mode chorus waves. *Journal of Geophysical Research: Space Physics*, 120, 7728–7736. <https://doi.org/10.1002/2015JA021562>
- Miyoshi, Y., Shinohara, I., & Jun, C.-W. (2018). The level-2 orbit data of Exploration of Energization and Radiation in Geospace (ERG) Arase satellite, Version v03. ERG Science Center. Institute for Space-Earth Environmental Research, Nagoya University. <https://doi.org/10.34515/DATA.ERG-12000>
- Miyoshi, Y., Shinohara, I., Takashima, T., Asamura, K., Higashio, N., Mitani, T., et al. (2018). Geospace exploration project ERG. *Earth Planets and Space*, 70(1). <https://doi.org/10.1186/s40623-018-0862-0>
- NCEDC. (2014). Northern California Earthquake Data Center. UC Berkeley Seismological Laboratory. Dataset. <https://doi.org/10.7932/NCEDC>
- Ni, B., Thorne, R., Liang, J., Angelopoulos, V., Cully, C., Li, W., et al. (2011). Global distribution of electrostatic electron cyclotron harmonic waves observed on THEMIS. *Geophysical Research Letters*, 38, L17105. <https://doi.org/10.1029/2011GL048793>
- Ni, B., Thorne, R. M., Meredith, N. P., Horne, R. B., & Shprits, Y. Y. (2011). Resonant scattering of plasma sheet electrons leading to diffuse auroral precipitation: 2. Evaluation for whistler mode chorus waves. *Journal of Geophysical Research*, 116, A04219. <https://doi.org/10.1029/2010JA016233>
- Ni, B., Thorne, R. M., Shprits, Y. Y., & Bortnik, J. (2008). Resonant scattering of plasma sheet electrons by whistler-mode chorus: Contribution to diffuse auroral precipitation. *Geophysical Research Letters*, 35, L11106. <https://doi.org/10.1029/2008GL034032>
- Noll, C. E. (2010). The Crustal Dynamics Data Information System: A resource to support scientific analysis using space geodesy. *Advances in Space Research*, 45, 1421–1440. <https://doi.org/10.1016/j.asr.2010.01.018>
- Ogawa, Y., Kadokura, A., & Ejiri, M. K. (2020). Optical calibration system of NIPR for aurora and airglow observations. *Polar Science*, 26. <https://doi.org/10.1016/j.polar.2020.100570>
- Otsuka, Y., Ogawa, T., Saito, A., Tsugawa, T., Fukao, S., & Miyazaki, S. (2002). A new technique for mapping of total electron content using GPS network in Japan. *Earth Planet and Space*, 54(1), 63–70. <https://doi.org/10.1186/bf03352422>
- Oyama, S., Shinbori, A., Ogawa, Y., Kellinsalmi, M., Raita, T., Aikio, A., et al. (2020). An ephemeral red arc appeared at 68° MLat at a pseudo breakup during geomagnetically quiet conditions. *Journal of Geophysical Research: Space Physics*, 125, e2020JA028468. <https://doi.org/10.1029/2020ja028468>
- Pacific Northwest Geodetic Array (PANGA) (1996). GPS/GNSS network and geodesy laboratory: Central Washington University, other/seismic network. International Federation of Digital Seismograph Networks. <https://doi.org/10.7914/SN/PW>
- Perry, C. H., Grande, M., Hall, A. M., & Wilken, B. (1996). Statistical survey of dispersionless substorm injections observed by the CRRES MICS ion spectrometer. In E. J. Rolfe, & B. Kaldeich (Eds.), *International Conference on Substorms, Proceedings of the 3rd International Conference held in Versailles, May 12–17, 1996* (pp. 567). ESA SP-389. Paris: European Space Agency.
- Prölss, G. W. (2006). Subauroral electron temperature enhancement in the nighttime ionosphere. *Annals of Geophysics*, 24, 1871–1885. <https://doi.org/10.5194/angeo-24-1871-2006>

- Rees, M. H., & Roble, R. G. (1975). Observations and theory of the formation of stable auroral red arcs. *Reviews of Geophysics*, 13(1), 201–242. <https://doi.org/10.1029/rg013i001p00201>
- Rich, F. J., & Hairston, M. (1994). Large-scale convection patterns observed by DMSP. *Journal of Geophysical Research*, 99, 3827–3844. <https://doi.org/10.1029/93JA03296>
- Roach, F. E., & Roach, J. R. (1963). Stable 6300Å Auroral Arcs in Midlatitudes, Planet. *Planetary and Space Science*, 11, 523–545.
- Shinbori, A., Otsuka, Y., Sori, T., Tsugawa, T., & Nishioka, M. (2020). Temporal and spatial variations of total electron content enhancements during a geomagnetic storm on September 27 and 28, 2017. *Journal of Geophysical Research: Space Physics*, 125, e2019JA026873. <https://doi.org/10.1029/2019JA026873>
- Shiokawa, K., Hosokawa, K., Sakaguchi, K., Ieda, A., Otsuka, Y., Ogawa, T., & Connors, M. (2009). The optical mesosphere thermosphere imagers (OMTIs) for network measurements of aurora and airglow, future perspectives of space plasma and particle instrumentation and international collaborations. *AIP Conference Proceedings*, 1144, 212–215. <https://doi.org/10.1063/1.3169292>
- Shiokawa, K., Katoh, Y., Hamaguchi, Y., Yamamoto, Y., Adachi, T., Ozaki, M., et al. (2017). Ground-based instruments of the PWING project to investigate dynamics of the inner magnetosphere at subauroral latitudes as a part of the ERG-ground coordinated observation network. *Earth Planets and Space*, 69(1), 160. <https://doi.org/10.1186/s40623-017-0745-9>
- Shiokawa, K., Katoh, Y., Satoh, M., Ejiri, M. K., & Ogawa, T. (2000). Integrating-sphere calibration of all-sky cameras for nightglow measurements. *Advances in Space Research*, 26, 1025–1028. [https://doi.org/10.1016/s0273-1177\(00\)00052-1](https://doi.org/10.1016/s0273-1177(00)00052-1)
- Shiokawa, K., Katoh, Y., Satoh, M., Ejiri, M. K., Ogawa, T., Nakamura, T., et al. (1999). Development of optical mesosphere thermosphere imagers (OMTI). *Earth Planet and Space*, 51, 887–896. <https://doi.org/10.1186/bf03353247>
- Shiokawa, K., Miyoshi, Y., Brandt, P. C., Evans, D. S., Frey, H. U., Goldstein, J., & Yumoto, K. (2013). Ground and satellite observations of low-latitude red auroras at the initial phase of magnetic storms. *Journal of Geophysical Research: Space Physics*, 118, 256–270. <https://doi.org/10.1029/2012ja018001>
- Sori, T., Shinbori, A., Otsuka, Y., Tsugawa, T., & Nishioka, M. (2019). Characteristics of GNSS total electron content enhancements over the midlatitudes during a geomagnetic storm on November 7 and 8, 2004. *Journal of Geophysical Research: Space Physics*, 124, 10376–10394. <https://doi.org/10.1029/2019JA026713>
- Spence, H. E., Reeves, G. D., Baker, D. N., Blake, J. B., Bolton, M., Bourdarie, S., et al. (2013). Science goals and overview of the Radiation Belt Storm Probes (RBSP) Energetic Particle, Composition, and Thermal Plasma (ECT) suite on NASA's Van Allen Probes mission. *Space Science Reviews*, 179, 311–336. <https://doi.org/10.1007/s11214-013-0007-5>
- Takagi, Y., Shiokawa, K., Otsuka, Y., Connors, M., & Schofield, I. (2018). Statistical analysis of SAR arc detachment from the main oval based on 11-year, all-sky imaging observation at Athabasca, Canada. *Geophysical Research Letters*, 45, 11539–11546. <https://doi.org/10.1029/2018gl079615>
- Thébault, E., Finlay, C. C., Beggan, C. D., Alken, P., Aubert, J., Barrois, O., et al. (2015). International geomagnetic reference field: The 12th generation. *Earth, Planets and Space*, 67, 79. <https://doi.org/10.1186/s40623-015-0228-9>
- Thorne, R. M., Ni, B., Tao, X., Horne, R. B., & Meredith, N. P. (2010). Scattering by chorus waves as the dominant cause of diffuse auroral precipitation. *Nature*, 467, 943–946. <https://doi.org/10.1038/nature09467>
- Tsyganenko, N. A., & Sitnov, M. I. (2005). Modeling the dynamics of the inner magnetosphere during strong geomagnetic storms. *Journal of Geophysical Research*, 110(A3), A03208. <https://doi.org/10.1029/2004ja010798>
- Wang, B., Li, P., Huang, J., & Zhang, B. (2019). Nonlinear Landau resonance between EMIC waves and cold electrons in the inner magnetosphere. *Physics of Plasmas*, 26, 042903. <https://doi.org/10.1063/1.5088374>
- Wang, S.-Y., Kazama, Y., Jun, C.-W., Chang, T.-F., Hori, T., Miyoshi, Y., & Shinohara, I. (2018). *The LEPe instrument level-2 omni-directional flux data of Exploration of energization and Radiation in Geospace (ERG) Arase satellite, Version v02.02*. ERG Science Center, Institute for Space-Earth Environmental Research, Nagoya University. <https://doi.org/10.34515/DATA.ERG-04002>
- World Data Center for Geomagnetism, Kyoto, Nose, M., Iyemori, T., Sugiura, M., & Kamei, T. (2015). *Geomagnetic AE index*. <https://doi.org/10.17593/15031-54800>
- Yokota, S., Kasahara, S., Hori, T., Keika, K., Miyoshi, Y., & Shinohara, I. (2018). *The MEP-i instrument Level-2 3-D flux data of Exploration of energization and Radiation in Geospace (ERG) Arase satellite, Version v01.02*. ERG Science Center, Institute for Space-Earth Environmental Research, Nagoya University. <https://doi.org/10.34515/DATA.ERG-03000>
- Yokota, S., Kasahara, S., Mitani, T., Asamura, K., Hirahara, M., Takashima, T., et al. (2017). Medium-energy particle experiments-ion mass analyzer (MEP-i) onboard ERG (Arase). *Earth Planets and Space*, 69, 172. <https://doi.org/10.1186/s40623-017-0754-8>
- Yuan, Z., Xiong, Y., Huang, S., Deng, X., Pang, Y., Zhou, M., et al. (2014). Cold electron heating by EMIC waves in the plasmaspheric plume with observations of the Cluster satellite. *Geophysical Research Letters*, 41, 1830–1837. <https://doi.org/10.1002/2014gl059241>
- Zhou, Q., Xiao, F., Yang, C., He, Y., & Tang, L. (2013). Observation and modeling of magnetospheric cold electron heating by electromagnetic ion cyclotron waves. *Journal of Geophysical Research: Space Physics*, 118, 6907–6914. <https://doi.org/10.1002/2013ja019263>